Imaging the Ionization Track of Alpha Recoils for the Directional Detection of Weapons Grade Plutonium

by

William Lawrence Koch

B.S., Physics
United States Military Academy (2004)

Submitted to the Department of Physics
in partial fulfillment of the requirements for the degree of

MASTER OF SCIENCE IN NUCLEAR PHYSICS

at the

MASSACHUSETTS INSTITUTE OF TECHNOLOGY

June 2013

Author .....
Department of Physics
May 8, 2013

Certified by .. ..
Peter Fisher
Division Head, Laboratory of Nuclear Sciences
Thesis Supervisor

Accepted by .....
John Belcher
Associate Department Head for Graduate Education

Imaging Alpha Recoils for the Directional Detection of Weapons Grade Plutonium

by

William Lawrence Koch

Submitted to the Department of Physics
on May 1, 2013, in partial fulfillment of the
requirements for the degree of
MASTER OF SCIENCE IN NUCLEAR PHYSICS

Abstract

Since the dawn of the nuclear weapons era, political, military, and scientific leaders around the world have been working to contain the proliferation of Special Nuclear Material and explosively fissile material. This paper describes the construction of a prototype, directional, fast neutron detector, modeled after the Dark Matter Time Projection Chamber. Fast neutrons are emitted by a host of interesting sources, including medical isotopes, research sources, cosmic neutron spallation, and the most interesting, SNM and WGP. This detector was built for remote operations using a computer terminal for the detection of Special Nuclear Material (SNM) and Weapons Grade Plutonium (WGP). Further, this paper discusses the baseline and characterization testing using a low intensity Americium-Berillium neutron source, compared with probability-based rate calculations and Geant4 simulation rates. The detector, in its current configuration agrees well with the expected rates, showing a 95% track reconstruction effiency, computed from both the probability-based rate calculation and the Geant4 simulation rates. Scaling this to an appropriate size, this detector provides an entirely unique and new piece of information in the world of radiation detection: direction to fast neutron source. The primary concept of employment focuses on building statistics through large total cross section, increased scan time, or proximity of scan source. With these three variables balanced for a specific operational environment, this detector technology is able to pinpoint fast neutron sources in a wide variety of scenarios.

Thesis Supervisor: Peter Fisher
Title: Division Head, Laboratory of Nuclear Sciences

Acknowledgments

I would first like to thank the Creator for giving us such an interesting Physics equation, always at the edge of our fingertips, but forever infinitely out of reach.

Professor Fisher, for his undeniable patience in bringing me up to speed with the world of scientific research. I take it as absolute my experience here has been fruitful and rewarding because of your patience and understanding for my unique set of skills (which had very little to do with scientific research upon arrival).

Professor Rajagopal, for honest and helpful guidance with a once-in-a-lifetime transition from flying helicopters in the desert to physics classes at MIT in less than three months.

The Department of Physics and Nuclear Engineering at West Point, for providing me the opportunity to attend this great institution.

Howard Choe and Jim Pruett of Raytheon for funding this prototype detector research and helping upgrade for the characterization testing.

The Defense Threat Reduction Agency for creating and funding the research for prototype radiation detectors.

The Institute for Soldier Nanotechnology for funding the initial construction of this detector.

The Dark Matter Time Projection Chamber collaboration for allowing me to join after years of hard work and take this technology in a new route.

My office mates, Shawn, Jeremy, and Cosmin. I averaged roughly a half dozen questions a day, for approximately 20 months. Most of the code presented in this paper was originally written by these three, blasted into pieces by me, re-written by them, and finally presented in this paper. It is not just the results of their hard labor, it is the results of their hard labor, squared.

My classmates, Ian, Alex, and Doga. There were many times they carried me through problem sets. By many, I mean every problem set we were assigned.

My parents, sister, brother, and brother-in-law, for teaching me to believe. And then reminding me once a week so I don't forget.

Most of all my wife and two kids. Where MIT taught me true humility, my family teaches me year in and year out true happiness.

THIS PAGE INTENTIONALLY LEFT BLANK

Contents

List of Figures

THIS PAGE INTENTIONALLY LEFT BLANK

List of Tables

THIS PAGE INTENTIONALLY LEFT BLANK

Chapter 1

Introduction

Sir,

Some recent work by E. Fermi and L. Szilard, which has been communicated to me in manuscript,leads me to expect that the element uranium may be turned into a new and important source of energy in the immediate future...

Signed

A. Einstein

Letter to President Roosevelt[1]

On July 16th, 1946, the United States detonated the first nuclear warhead[2]. Known as the "Trinity Event", the explosion witnessed a yield equivalent to ten thousand pounds of TNT using a plutonium implosion design [3]. Less than three weeks later, the first uranium gun-type warhead was dropped on Hiroshima, followed in three days by another plutonium implosion device on Nagasaki, both resulting in similar explosive yields [2]. These three events were the dawn of the nuclear weapons era.

1.1 The Road to Chain Reaction

The discussion of detecting Special Nuclear Material (SNM) and plutonium warheads should begin at the beginning, with the discovery of fission. In Rome during the first half of the 1930s, Enrico Fermi was conducting experiments bombarding various nucleii with neutrons when his team discovered the effects of properly chosen moderator to increase the probability of interaction [4]. After working up the periodic table, Fermi's team witnessed unexpected results when observing the reactions of thermal neutrons on a uranium target. This phenomenon was the birth of nuclear fission. Knowing the devestation that would arrive in only a few short years, it is an interesting note that his team improperly diagnosed the results while German scientists appropraitely termed this reaction as "nuclear fission" [4], giving both sides of World War II knowledge of this new phenomenon.

Fueled by rising tensions between different alliances, the following decade witnessed an unprecedented international race to acheive explosive fission chain reaction. Early in the development, ^{235}U, occuring naturally and having a large thermal neutron cross section, was found to be the "only meta-stable isotope of uranium that is fissile" [4]. However, this implied separating ^{235}U from the naturally occuring ^{238}U using nothing more than the mass difference. Two sides formed, with Niels Bohr even stating "With present technical means it is ... impossible to purify the rare uranium isotope to realize the chain reaction" [4]. Within a few years, multiple isotopes were found to be fissile, with ^{239}Pu the only other fissile isotope reasonably capable of being separated from naturally abundant isotopes..

As World War II picked up ferrocity and multiple nations were seeking to achieve explosvie chain reaction, processes were developed to produce significant quantities of ^{235}U and ^{239}Pu. Since the discovery of fission, two general material processes had evolved to isolate these fissile isotopes: uranium enrichment to achieve Highly Enriched Uranium (HEU) and uranium irradiation with chemical re-processing to

produce Weapons Grade Plutonium (WGP). Although more isotopes are capable of sustaining nuclear fission chain reaction, these processes would require much more technological development even in modern standards and will therefore not be considered for the context of this discussion.

Both uranium enrichment and plutonium production are technologically difficult processes, each with unique considerations. The primary fissile isotope, ^{235}U, occurs with only 0.7% ^{235}U abundance and the remainder predominantly ^{238}U. This requires enrichment to bring the isotope percentage above 20%. Historically, uranium enrichment was guarded behind a curtain of high costs and technological feats. The enrichment process in the United States has traditionally been conducted in massive gaseous diffusion plants, requiring an astronomical supply of electricity and robust cooling towers. The U.S.S.R.successfully used centrifuge technology throughout the second half of the 20th century. A common understanding of centrifuge technology indicates a need for advanced knowledge of high-speed rotating mechanical design. These centrifuges and diffusion plants were often thought to be too far advanced (both technologically and financially) for rogue nations or terrorist groups, but the dawn of open information and internet resources has opened the realm of possibilities to these groups for domestic small-scale enrichment facilities. Further, newer designs for uranium enrichment are under development, which may open the doors for "basement-sized" uranium enrichment.

The production of WGP follows a similar path of difficulty but along a different course. Plutonium does not occur in abundance on Earth, and therefore must be produced through neutron irradiation of ^{238}U. After the uranium absorbs a neutron, the ^{239}U decays by beta decay for two iterations through ^{239}Np arriving at ^{239}Pu. This presents two technologically difficult operations: 1) Operating a nuclear reactor and 2) Chemically re-processing Spent Nuclear Fuel (SNF) to remove significant quantities of short-lived daughter isotopes. The former is becoming a much more achievable pro-

Isotope	Bare Critical Mass
^{233}U	16
^{235}U	52
^{238}Pu	10
^{239}Pu	10
^{240}Pu	40
^{241}Pu	10
^{242}Pu	100

Table 1.1: Critical masses for fissile uranium and plutonium isotopes

cess, as nuclear reactors are continuing to become a wide spread method of electricity production. The chemical re-processing has long been thought to be the primary barrier to plutonium warhead proliferation, but in 1993, J. Carson Marka published a paper discussing the various isotopes of plutonium and their use in warhead construction [5]. Table 4.1 presents bare critical masses from Mark's study on plutonium. This table also presents HEU critical masses from the Nuclear Weapons archive[6] for reference.

The result of Marka's study show that even plutonium taken directly from a nuclear reactor could foreseeably be used in a nuclear weapon similar to a uranium weapon [5]. The critical masses are similar for contamination isotopes of plutonium, inferring the weapon would be similar in size to a weapon with a uranium core at sub-optimal isotopic percentages. This indicates a possible route to proliferation could be nothing more than smuggling spent nuclear fuel from reactor plants.

The processes involved for each material differ from the material's production to the size and design of the nuclear warhead. The primary driving factor for enrichment/irradiation processes and warhead design is the critical mass. The critical mass of a substance is determined by the neutron cross sections and the density of the material. To achieve a nuclear chain reaction, the starting ingredient is a nuclear isotope that fissions upon impact of a thermal neutron, producing one or more neutrons. These neutrons have a certain probability of reaching the surface of the mass, while

the difference is "consumed in fissioning other nuclei" [7]. The larger the mass, the lower the probability of escape, and therefore the higher the probability of inducing fission on other nuclei. With sufficient mass, the "number of neutrons that fail to escape will number enough to fission every nucleus in the sample" [7]. This mass is known as the critical mass, and is the driving force behind enrichment or neutron irradiation to produce the two most common explosively-fissile materials, HEU and WGP. The size of payload is determined by the weapon delivery type, which therefore determines the allowable size of the fissile material. The size capability of the fissile material determines the amount of enrichment/irradiation of raw materials.

Nuclear weapons must quickly acheive and momentarily maintain the critical mass to sustain the chain reaction on the time scale of a weapon detonation. Further, percentage of enrichment or percentage of particular isotopes in the final material determines the mass of the warhead. Therefore, with a higher percentage of ^{235}U or ^{239}Pu, a smaller mass is capable of attaining explosive chain reaction. This can be further reduced by adding neutron reflector material, which not only reflects neutrons back into the fissile mass, it allows slow the rate of explosion, allowing more nucleii to time to fission. Although the neutron reflector may be consumed in the fission chain reaction, it is generally not a fissile material by itself. It does, however, have a high total neutron cross section, forcing a greater number of neutrons that would otherwise escape the mass to be reflected. For reasons discussed in the next section, HEU is predominantly employed through the gun-type warhead assembly due to the higher mass needed to acheive the critical mass, while WGP is only capable of explosive chain reaction in implosion type weapons. Although uranium is capable of explosive fission in an implosion type design, the material required would be formidible. WGP is known to require a smaller mass of material to achieve the nuclear chain reaction, allowing critical masses on the scale of 4 kilograms. In a study to determine the feasibility of detecting nuclear warheads, Fetter *et al.* determined the smallest neutron

reflectored mass of fissile material capable of achieving explosive chain reaction was 12 kg of uranium or 4 kg of plutonium both in an implosion-type weapon, with the ^{235}U enriched to 93.3% and ^{239}Pu isotopic percentage of 93.3%, respectively[8].

Inevitably, the lowest accepted mass for the construction of a nuclear weapon is through the use of WGP surrounded by a neutron reflector, resulting in a critical mass of 4 kilograms. This is roughly the size of a softball, not including the surrounding materials, and approximately nine pounds. Including an appropriate reflector, tamper, explosives and casing, the size jumps to 21 cm radius, or better, a 280 pound, 16" medicine ball[10].

1.2 Devices Supporting Nuclear Detonation

There are two broad categories of nuclear weapons: fission bombs and fusion bombs. The former produces explosive power many orders of magnitude greater than chemical explosives while the latter adds many orders more. The typical explosive yield of a fission-only weapon is on the order of tens to a hundred of kilotons TNT-equivalent, while fusion devices reach as high as 50 megaton [9]. While the name implies two completely separate processes, the truth is that all fusion designs use a fission chain reaction to start the explosive fusion chain reaction. For this reason, all nuclear weapons derive themselves in some form from the fission reaction.

The fission chain reaction is theoretically supported by a wide range of isotopes, but has only been technically developed world-wide for two primary isotopes: ^{235}U and ^{239}Pu. Their are two general devices that support the fission chain reaction for these isotopes: gun-type and implosion. The primary function of each design is to bring a sub-critical mass of fissile material to a super-critical mass and initiate an explosive chain reaction with a blast of neutrons. The gun-type device accomplishes this task by firing an enriched, sub-critical plug of uranium at another enriched,

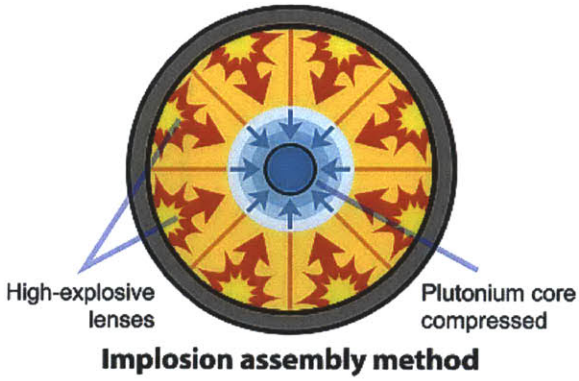

Figure 1-1: An example of an implosion device from the Comprehensive Nuclear-Test-Ban Treaty Organization website, depicting plutonium core, neutron reflector, tamper, and explosives[9]

sub-critical mass of uranium [9]. The gun portion of the device is nothing more technical than standard artillery firing, only with short, light barrels and expendable compoments [11]. When the two masses meet, super-critical mass is achieved and the fission chain reaction commensurates. This design is the simplest nuclear weapon, but is also the least efficient and bulkiest [9]. The Little Boy gun-type bomb used in World War II was approximately 1.1% efficient, with an appoximate 12-kt yield for a 64-kg, 9.4 cm radius uranium core and 18cm radius tungsten-carbide tamper [7]. This is compared to the expected yield of pure ^{235}U at 17.6 kt/kg [7]. Further, WGP is not feasible for use in the gun-type assembly due to criticality issues [8]. Due to the increased amount of HEU required to acheive critical mass as well as the mechanical construction of the gun-type assembly, the resulting weapons payload is considerably larger. More significantly to the application of the current work, there is minimal neutron signal, as presented in the previous section. Therefore, the bulky, inefficient gun-type assembly will not be discussed further in this paper other than to say, gun-type assemblies would be extremely difficult to smuggle across borders.

The alternate method of acheiving explosive criticality is through an imploding mass of plutonium, shown in Fig. 1-1. The implosion device is considered to have greater efficiency and yield in a smaller package [9]. This design uses two shells

of WGP, generally surrounded by one layer of neutron reflector, one layer of tamper material, and one layer of explosives. The design makes use of the "plastic flow tamper and active material under high-explosive impact" [11]. As discussed earlier, the use of tamper material provides the ability to reduce the total mass of WGPu to 4 kilograms through neutron reflection. Additionally, with no need for a bulky gun barrel in the construction design the assembly is smaller still. The implosion process is simple to explain and has traditionally been difficult to construct. The foundational principle is to create a super critical mass through imploding a spherical mass of WGPu (hollow or solid) [9]. Historically, the most difficult step is creating the uniform shock wave surrounding the plutonium mass, known as explosive lensing. However, "experts te the Nuclear Control Institute warn that it could still be accomplished by a small group of people with the right training and experience if they have access to plutonium"[9]. In other words, the difficult engineering may no longer be out of reach to rogue nations or terrorist organizations. A second historical safeguard point is the concept of requiring a test for implosion type weapons. Again, however, terrorist organizations, and possibly even rogue nations, may not require a full yield and be happy with a minimally efficient explosion. All aspects considered, Fetter *et al.* placed a lower bound on the number of neutrons emitted from a fully constructed (tamper material included) plutonium warhead: 400,000 neutrons/second [8]. This weapon involved the lowest accepted mass for the construction of a nuclear weapon: a WGP core just below the critical mass of 4kg and surrounded by a reflector, tamper, and explosives. The plutonium core is roughly the size of a softball and approximately nine pounds. Including an appropriate reflector, tamper, explosives and casing, the size jumps to 21 cm radius, or better, a 280 pound, 16" medicine ball[10].Another study also published an estimated intensity of plutonium warheads (using U.S. "Super-Grade Plutonium," with only 2% ^{240}Pu) of 150,000 neutrons/second [12]. Further, both reports agree on the Watts spectrum of neutron energies centered on approximately 1MeV, depicted

in more detail for ^{252}Cf. The result is a detectable signal of fast neutrons, even at the lowest limit, with rogue nations and terrorist organizations more than likely possessing weapons with much higher intensity neutron signals due to ^{240}Pu contamination.

1.3 The Rise of Non-Proliferation Initiatives

The early stages of the nuclear weapons era witnessed the spread of these devastating devices to multiple nations within a few years. Dubbed the "Nuclear Arms Race," the world's superpowers were adamant on acquiring, testing, and maintaining an arsenal of nuclear weapons for self defense. On a parallel track, many of the world's leaders recognized the true danger of an abundance of nuclear weapons and weapons building knowledge. These leaders, scientific, military, and political, even began their work on non-proliferation initiatives prior to the first detonation.

By 1946, the leaders of the United States had already grown weary about the proliferation of nuclear arms. While giving his initial brief to President Truman of the existence of the secretive Manhattan Project, Secratary of War Henry Stimson noted "both great dangers and great opportunities"[13]. Stimson went on to describe that "the future may see a time when such a weapon may be constructed in secret and used suddenly and effectively with devastating power by a wilful nation or group against an unsuspecting nation or group of much greater size and material power" [14]. Less than a year after the bombings on Japan, many atomic scientists assembled into a body known as the "Emergency Committee of Atomic Scientists," and was founded with six principles, one of which states "international control of atomic energy and, ultimately, the elimination of war, is the only solution to the problem" [15]. This committee included notable scientists such as Einstein, Urey, Bethe, Szilard, and Weisskopf.

Approximately one year after the Trinity event and the two nuclear weapons were

detonated in Japan, the United States proposed the "Baruch Plan" to the United Nations. The Baruch Plan, name after the man presenting the plan to the United Nations, was a proposal that "called for the bringing of all forms of atomic energy under the control of an agency of the United Nations" [13]. This plan was not accepted for reasons that have been debated over the last 60 years, but it succeeded in planting a framework for an agency created seven years later following proposals by President Dwight D. Eisenhower. In 1953, President Eisenhower addressed the General Assembly of the United Nations suggesting governments to unite and make "join contributions from their stockpiles or normal uranium and fissionable materials to an International Atomic Energy Agency... set up under the aegis of the United Nations" [16]. With this speech was the first successful attempt at an international organization for managing atomic energy, dawning the era of the International Atomic Energy Agency (IAEA).

After a shakey start and decades-long battles over the tracking of fissile materials, the present model for the IAEA revolves around the notion of non-nuclear-weapon member states adhering to safeguards, or a "system of materials accountancy, containment, and surveillance administered by the IAEA and supported by regular onsite inspections at declared facilities" [17]. In addition to this system of inspections, the IAEA defines amounts of nuclear material as "significant" if the "approximate quantity of nuclear material in respect of which, taken into account any conversion process involved, the possibility of manufacturing a nuclear explosive device cannot be excluded" with significant quantities defined as 8kg plutonium or 25 kg of uranium [18].

In addition to the positive tracking of nuclear materials through the international efforts of the IAEA, the United States also maintains an thorough detection program at all ports of entry. This is often referred to as a defense in depth, with the first line of defense "locking down nuclear materials in the former Soviet Union" [19]. This

is described by an 11-layer system, with the first seven layers being certification, seals, and alarms. The final four are inspections, and three of these inpsections being radiological detection systems[20].

For the last few decades, the methods of detecting nuclear weapons and special nuclear material at ports of entry, border crossings, airports, and declared nuclear facilities relied on both the gamma ray spectrum and the neutron spectrum of plutonium and uranium. HEU contains more than 20% U-235, the primary nuclear-chain-reaction supporting isotope. However, the smaller the warhead, the higher the enrichment. In other words, the concerns for materials being covertly transported into the United States (or around the world for that matter) are less focused on a 2,000 kilogram 20% enriched nuclear warhead. This type of warhead will set off multiple x-ray alarms, scales, and visual inspections prior to needing a specialized radiation detector. However, a 93% ^{235}U core warhead that is a total mass of 180kg and could foreseeably fit in a large suitcase or crate would be a much greater concern. Similarly, plutonium's critical mass decreases as the percentage of ^{239}Pu increases. However, the ability to completely remove the principle contamination isotope, ^{240}Pu is essentially impossible, with the lower limit generally accepted as 6% ^{240}Pu. With this high of a percentage of ^{239}Pu, the critical mass could be as small as four kilograms, as discussed in previous sections. This, with tamper included, could fit inside of a small suitcase, or even easier, could fit in a crate in the center of cargo container. These two scenarios provide the lower bounds for construction of radiation detectors.

1.4 Searching for Fast Neutrons

A defense is only as good as the weakest link. The current market for gamma ray detectors is astounding, with novel approaches to provide directionality and detection at a distance. However, the prospects for neutron detectors are less than desireable.

The current technology focuses on a few isotopes and the monstrous thermal neutron cross section. With isotopes such as ^{3}He and ^{10}B sitting around 5,300 and 3,835 barns respectively for thermal neutrons, focusing on these isotopes is somewhat understandable [21]. At portal monitors across the globe, the International Atomic Energy Agency and host nation inspection teams use the gamma spectrum and moderated neutron spectrum to monitor the flow of Special Nuclear Material. The question becomes: Is a moderated neutron signal the optimal resource for plutonium SNM tracking? Information is destroyed the moment the neutrons are moderated, leaving nothing more than a proporitional counter with zero directionality. Further, several joint studies between the United States and the U.S.S.R. were conducted in the late eighties and published in the early nineties hinting at the need to collimate a neutron detector to provide detection at a maximal distance [8]. The detector tested in this work measures the minimally moderated signal of fast neutrons emitted by an Americium-Beryllium induced fission neutron source.

The neutrons emitted from WGP and Special Nuclear Material are predominantly the result of the spontaneous fission of ^{240}Pu. Spontaneous fission occurs as a result of a fraction of the nucleus quantum tunneling through the nuclear strong force barrier. Further, the heavier isotopes have higher neutron-to-proton ratios, resulting in multiple neutrons being emitted during the fissioning process, when two fragment nucleii are emitted with higher than normal neutron-proton ratios. These neutrons are emitted with a range of energy with the majority of energies occuring around 1 MeV, as depicted in Fig. 1.4:

For current neutron detection technologies, the target material's sensitivity generally lies below 0.1 MeV in the thermal neutron energy realm, requiring a moderator to be built into the detector. Once the moderation shield is emplaced, the detector is only sensitive to a narrow band of energies. The higher end of the spectrum will not lose enough energy prior to passing through the thermal neutron detector, and

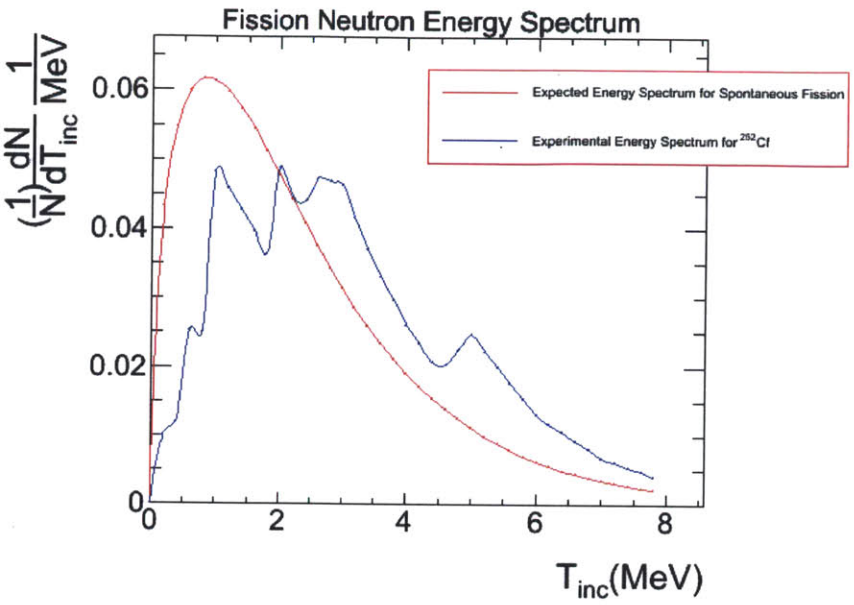

Figure 1-2: The expected spontaneous fission spectrum computed as a Watts Spectrum with numbers from ENDL is compared with an experimental ^{252}Cf fission neutron energy spectrum[22]

the lower end of the energies will not make the trip through the moderation material. A common relationship between neutron detectors is known as intrinsic efficiency. Intrinsic efficiency is the percentage of neutron interactions given a flux of neutrons through the detector. Although the thermal neutron detectors have a favorable intrinsic efficiency for specific energy ranges, the narrow band of acceptance prior to entering the detector is rarely discussed as a limiting capability. The resulting total intrinsic efficiency is generally on the order of 10%[8].

The detector tested in this experiment has a theoretical intrinsic efficiency of approximately one percent, depending on particular set-up. This will reduce the number of neutron interactions within the sensitive volume. However, the traditional detectors do not provide a direction-sensitive measurement. Operating at a reduced intrinsic efficiency is compensated for by providing directionality. Therefore, the discussion of using a heavily shielded neutron detector as a means of collimating the signal (and thereby ignoring background cosmic-ray induced neutrons) is immediately built into

this directional detector. Instead of moving heavy shielding as the detector moves, the software is built to only observe signals above an isotropic cosmic-ray induced neutron background. Finally, this detector, in contrast to current technologies, is insensitive to gamma radiation, thereby reducing false alarms from background radiation transients[23].

1.5 Introduction - Closing Argument

The trafficking of plutonium and uranium are both significant threats to the United States and the world in general. Quantities as small as four kilograms of plutonium could be assembled into a nuclear warhead and detonated with a yield of ten kilotons TNT-equivalent, destroying a modern metropolitan area. The current approach to monitor border crossings, inspect nuclear facilities (power and material handling), and inspecting ports of entry present a strong framework in the efforts to prevent nuclear proliferation. However, the fast neutron signal is the final hole in the defense that needs to be addressed. This paper presents the results of testing a prototype fast-neutron detector that may solve this problem.

Chapter 2

Experiment Setup

I have no special talents. I am only passionately curious.

A. Einstein[24]

2.1 Theory

The work presented in this paper was conducted using the technology developed by the Dark Matter Time Projection Chamber (DMTPC) Collaboration[25, 23, 26]. The detector is a modern twist on a classic technology. Time projection chambers were first created in 1974 and within ten years termed the "bubble chamber of the 1980s and 1990s" [27]. The physics of time projection chambers continues to thrive as some of the world's major experiments incorporate this classic detector. This section provides a brief introduction to Time Projection Chambers and the unique considerations made to the directional detection of fast neutrons from SNM and WGP, including the reasons for choosing specific gas mixtures and the possibility of detection at a distance. In closing, a thorough description of the construction of this prototype detector is presented.

2.1.1 Time Projection Chambers

The basic construction of this detector is a classic detection technology for the world of high energy physics. The central focus of this technology is of ionization tracks, or a string of electrons liberated by an energetic charged particle streaking through the active target volume. The "Time Projection Chamber" (TPC) broadly describes a detector that uses a two-dimensional ionization track reconstruction and the amount of time the track of electrons takes to cross the amplification region to build the magnitude of the third dimension of the track[27]. Further, the amount of charge collected directly correlates to the total ionization of the charged particle's track. The final result gives a three-dimensional understanding of the charged-particle track and the initial energy of the charged particle, or the recoil energy. The application of this techonology to the detection of WGPu derives from the DMTPC collaboration. The collaboration uses a host of modern technology built into the design of their TPC to arrive at a directional detector with an energy threshhold for directionality of approximately 80KeV nuclear recoil[25].

The flow of physics in a typical TPC are as follows (depicted in Fig. 2-1): 1) an energetic charged particle creates a track of electron-ion pairs; 2) the track of electrons drift in a low, uniform electric field to an amplificatoin region; 3) the track is read out at the amplification region retaining spatial information; 4) charge-readout provides temporal information to construct the third dimension. The ability to create large volumes of target gas while retaining directional information make this technology extremely beneficial to rare-event searches, giving these collaborations the possibility of large sensitive volumes[27]. Specific to the current experiment, a 50 liter chamber produces a target volume of 35 liters at 1.5 atmosphere, with growth room to achieve 45 liters and 5 atmosphere. Increasing pressure increases the total number of target nucleii while adversely affecting the nucleii recoil distance. With the proper combination of lens and camera offering resolution in the region of 100s of micrometers,

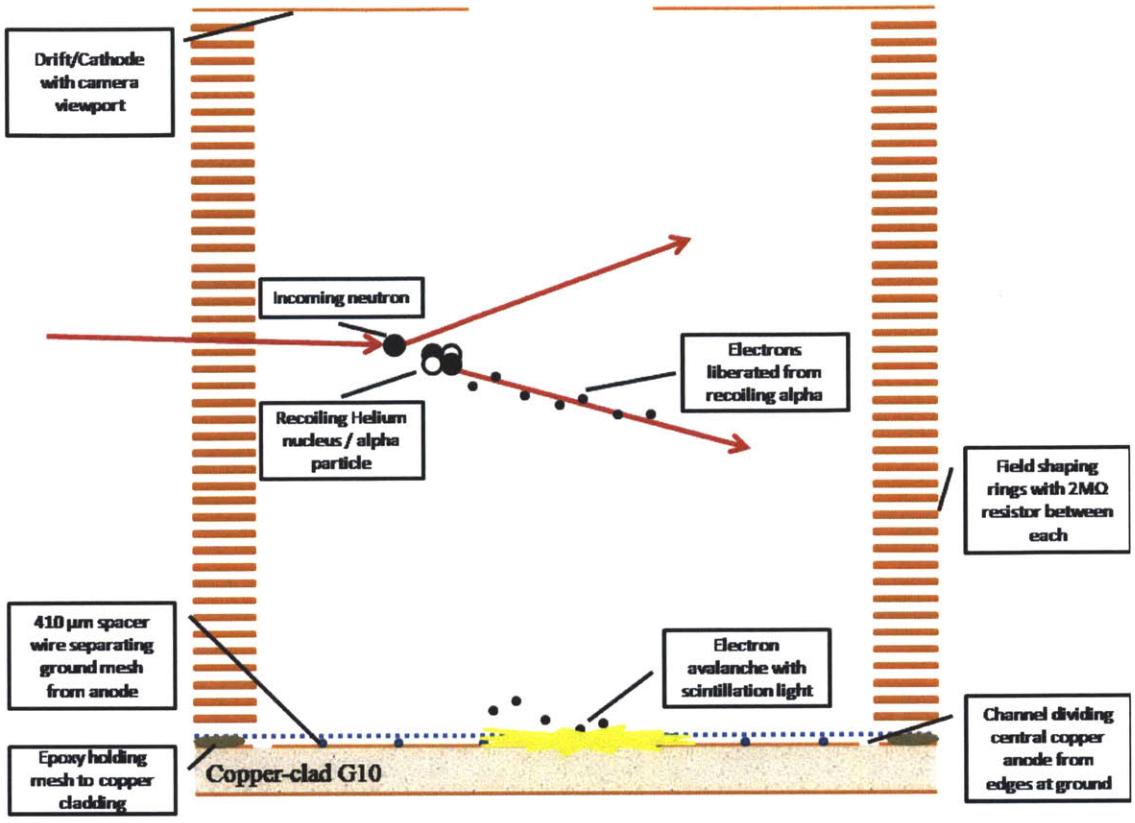

Figure 2-1: A cartoon diagram of the Time Projection Chamber used in this experiment

pressures of five atmosphere are entirely within reach for operational detectors. Further, the experiment being discussed was conducted in order to demonstrate a 50-cm drift for the electron ionization tracks, while retaining directional information.

2.1.2 Ionization Track Characteristics

The charged particle's ionization energy is driven by the gas characteristics and the type of charged particle. The work function of specific molecules are the driving factor in the creation of electron-ion pairs for the recoiling charged particle. The target gas must provide a source of molecules which ionize with a low energy and witness minimal diffusion throughout the length of drift to the amplification regin. The two gases chosen for this detector technology, Helium and TetraFlouromethane

(CF_4), both exhibit optimal properties in regards to the work function. Studies show that the work function for CF_4 is approximately 34eV[28, 29] and for Helium is approximately 40eV depending on contamination [30].

The electrons liberated in the ionization process are drifted in the uniform electric field towards the amplification region, with the gas characteristics effecting the diffusion of the track. As the electrons drift in the uniform electric field, scattering, electron atachment and particle interactions all affect the original track of electrons and are summed into the phenomenon of diffusion. The drift and diffusion of the ionization track is directly effected by the gas characteristics, the total drift distance, and the magnitude of the electric field. In Fig. 2-2, a DMTPC program was tailored to the drift distances used in the current experiment's context to portray the amount of diffusion expected over a 48 cm drift. The data input for the CF_4 and Helium diffusion calculation derives from papers written by Christophrou *et al.*[28] and Pack [31]. In Fig. 2-3 represents the diffusion of electrons in Helium expected when running at higher pressures as well as a 48 cm drift distance.

The type of readout determines the magnitude of the signal and the magnitude of the noise. Traditionally, multiwire proportional chambers were used to collect the ionization track information. However, the DMTPC collaboration demonstrated the use of micropattern detectors coupled with the scintillation light of CF_4[26, 25]. Further, the collaboration demonstrated the use of Helium as the target gas and CF4 as the quenching gas to increase the number of nucleii present in the sensitive volume of the detector, thereby increasing the total cross section of the detector [23]. The photons captured by the EMCCD camera are a result of the scintillation light from the CF4 molecules involved in the electron avalanche at the amplificatoin region. CF4 scintillates predominantly around 640 with a smaller peak centered on 300nm[32] and the EMCCD camera maintaining a 90% quantum efficiency between 350 and 700 nm.

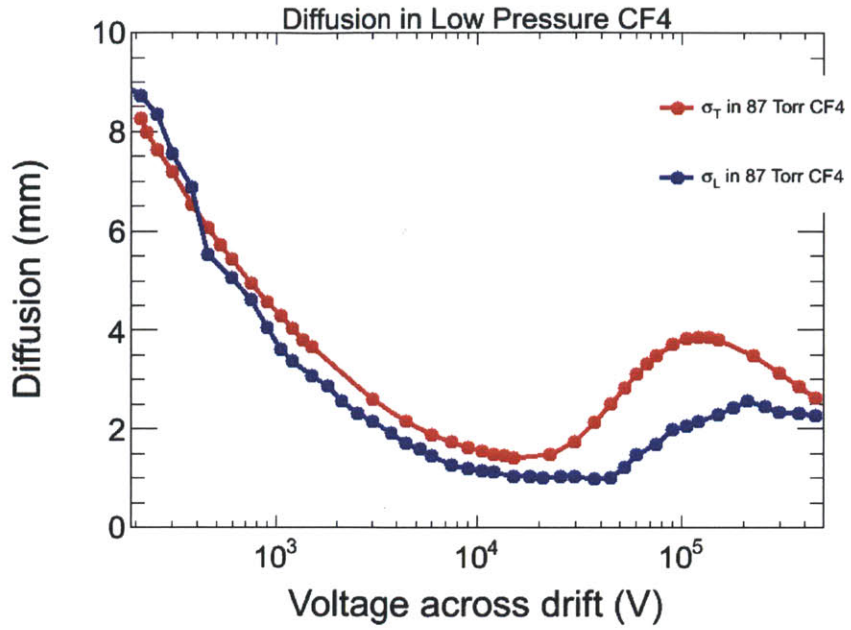

Figure 2-2: The expected longitudinal and transverse diffusion over 48cm of drift for 87Torr CF_4[28].

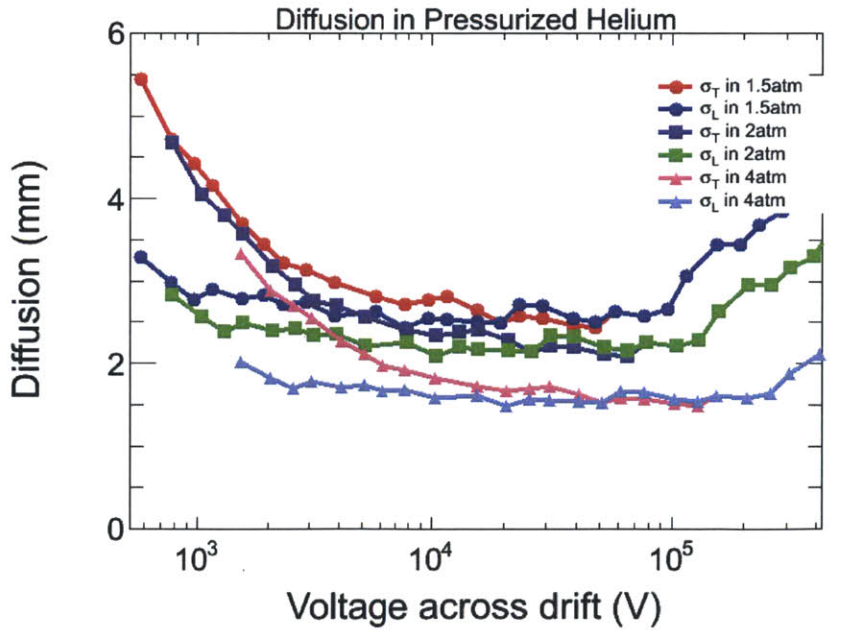

Figure 2-3: The expected longitudinal and transverse diffusion over 48cm of drift in various pressurized Helium settings[31].

2.1.3 Chamber Efficiencies and Detection at a Distance

In 1990, two reports were published describing the theoretical limits of detecting nuclear warheads at a distance[8, 12]. The studies were conducted jointly between the United States and the U.S.S.R. to improve the ability to monitor nuclear weapons bans and the proliferation of Special Nuclear Material. Both studies were in relative agreement with each other and jointly resulted in the understanding that detection of plutonium warheads at a distance can only be accomplished by the fast neutron signal.

In a Fetter *et. al.*'s report, the team places a lower limit on the intensity of neutrons emitted by WGP as 55,000 neutrons per second per kilogram[8]. This number, however, is extremely sensitive to isotopic percentage. Plutonium, as discussed earlier, is only produced in advanced nuclear weapons states at a "super-grade" of two percent ^{240}Pu, while typical WGP aligns with this studies numbers. Several years later, another report was published stating Reactor-Grade Plutonium may be used in quantities similar to ^{235}U, which would only increase the intensity of neutrons from the warhead [5]. Finally, the parallel report published by Geer in 1990 produces numbers similar to Fetter *et. al.*, with a slight decrease for moderation through the thick walls of a naval vessel [12]. For the extent of this paper, Fetter *et. al.*'s final number is used. The study presents a lower limit for neutron emission of a plutonium warhead of 400,000 neutrons/second regardless of tamper material [8].

In order to detect a warhead at a distance, there must be an understanding of the neutron background. Fetter *et. al.* presents a sea level neutron flux of $50m^{-2}s^{-1}$. The equation presented in Fetter's study,equation 2.1:

$$\frac{A_s \epsilon_s S}{4\pi r^2} = A_b \epsilon_b b \tag{2.1}$$

presents a rough calculation of the source signal versus background signal. Here,

A_s and A_b represent the area of the detector susceptible to the signal and background respectively, ϵ_s and ϵ_b the corresponding intrinsic efficiencies, and b the average background intensity, discussed earlier. The maximum distance between source and detector, r, is produced when the source signal is set equal to the background signal.In this report, the detectors are assumed to be collimated with certain data accumulation times. The results are, in agreement with Geer's report, detection of fast neutron signals out to 40 meters for larger detectors and one minute data accumulation [8]. The detector tested in this paper is not collimated, but provides directional sensitivity. Therefore, computer software is capable of re-creating the same concept of collimation without the issue of awkward, bulky neutron shields on multiple sides, top, and bottom of a traditional neutron detector. Further, the neutron flux at sea level is predominantly isotropic, while the ship-effect is assumed small on terrestial-based applications. Using an isotropic background, any point source signal will eventually accumulate as a peak in the specific direction.

ne

2.2 Pressurized Chamber

The primary sensitive volume of this experimental apparatus is a 50 liter stainless steel cylinder designed to withstand vacuum as well as pressures up to 5 bar, with an overpressure protection up to 6 bar. In this experiment, the chamber was limited to 1.5 bar for the purposes of certifications as well as vacuum gauge limitations. With the proper certification, phase II of this experiment will include runs at 5 bar. The chamber, depicted in Fig. 2.2, has a large lid that allows for the installation and removal of the drift field cage without disassembling the field cage itself. Further, the chamber has multiple ports for electrical feedthroughs, calibration sources, and potential upgrades to turbo pumps. The ports most commonly used are KF-25 ports,

with quick-connect clamps that hold a rubber o-ring with metal centering ring. Two of these ports are permanently dedicated to the fill gas and vacuum pump, with one port servicing each line. Both the vacuum line and fill line have remotely operated valves that are powered through the Synaccess power strip, which will be discussed later. Three ports are used for the electrical feedthroughs, with the feedthroughs built directly into the KF-25 cover. One port provides the high voltage power supply to the anode, with a possible expansion of a veto channel with the same high voltage power supply through the same port. The port next to the camera port houses the high voltage power supply for the field cage cathode. The port at the bottom of the chamber (or opposite the lid) provides the feedthrough for the ground reference to the channel surrounding the anode (or veto if installed). This ground reference feedthrough also houses a fast amplifier output for future upgrades to use a two-peak charge signal for further tagging of nuclear recoils and reducing of backgrounds.[33] This method has been tested and used in the DMTPC collaboration extensively and with great success [33]. On the large lid of the pressurized chamber, next to the cathode high voltage feed through, is the vacuum-quartz window for the camera.

A field cage is housed inside the pressurized chamber, with a cartoon, cut-away diagram depicted in Fig. 2-1. The cathode is constructed out of a copper plate with a six inch view port with 88% transparent stainless mesh holding a uniform 5 kV potential difference from ground[26]. From the cathode, 48 0.060" thick copper rings, spaced at .345" are mounted on acytel rods extending from cathode to anode. Each ring is electrically isolated from everything except for a two megaohm resistance to the ring on either side. The resistor provides a voltage step and forces the copper rings to act as field shaping rings, maintaining a uniform electric field for the length of the drift volume. These rings and the cathode sit 0.5" from the chamber wall, a dimension that will be increased for Phase II to allow for higher cathode voltage settings. The last field shaping ring sits 0.345" above an amplification region, depicted in Fig. 2-

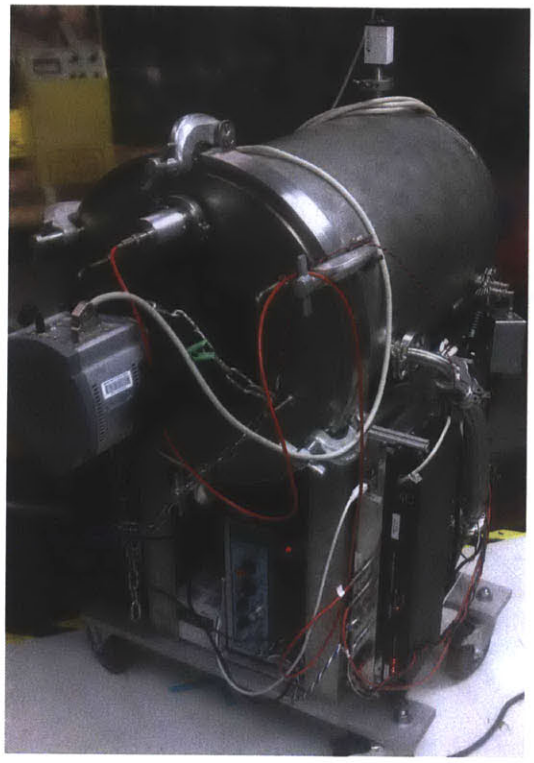

Figure 2-4: The 50-liter vacuum/pressure vessel that contains the sensitive volume, as well as the ports for camera see through, HV feedthroughs, and gas supply/exhaust lines.

Figure 2-5: The field cage comprised of the 0.060" copper field shaping rings, cathode with viewport, and field cage maintenance stand.

6. The anode was modeled after the DMTPC design, using $410 \pm 15\mu m$ insulated spacers to separate another 80% transparent stainless steel mesh from a copper clad G10 plate[26]. The G10 plate has a channel machined around the amplification region just inside the field shaping rings diameter to allow the mesh full contact at the edges with epoxy glue. The mesh was stretched to maximum tensile capability prior to being glued to the copper clad G10. This prevents any sag in the mesh due to electrostatic forces, which would otherwise result in a significant reduction in gain or potential shorting the anode to the ground-mesh. The spacers were originally installed every 1" and in later anodes installed at 2" as a result of increased tension in the mesh. The resulting amplification anode is capable of acheiving an electric field of 4.5kV/mm

in air, 1.75kV/mm in 75 Torr CF_4, and 1.82 kV/mm in 75 Torr CF_4 quenching gas with 1050 Torr Helium. The bottom of the field cage rests on metal feet which feed through a plastic hoisting plate. The plate is installed to remove the field cage for maintenance without placing excess stress on the field cage components and resistor chain. The metal feet place the backside of the copper clad G10 at ground with the vacuum vessel, which also serves as ground reference for the field cage.

Figure 2-6: This image shows the stretched 80% transparent mesh being glued on top of the $410\mu m$ spacers. Additionally, the machined channels can be seen beneath the mesh around the edge of the copper clad G10.

2.3 Image Processing System

The image processing system was tested with two cameras and multiple lenses. The first camera, and current setup, was a low-noise, fast readout Andor iXon 888 Electron Multiplying Charge Coupled Device (EMCCD) Camera with a 1 Mega Pixel (MP) chip[34]. The second camera tested was a Finger Lakes Instruments (FLI)

ProLine PL09000 standard Charge Coupled Device (CCD) camera with a 9.3MP chip[35]. Both cameras had similar pixel sizes ($13\mu m$ and 12 μm respectively), indicating an immediate nine times increase in imaging area in switching to the FLI ProLine camera. While the two cameras were tested for use with this detector set-up, the FLI ProLine proved insufficient. The primary purpose of this detector is providing real-time information about a neutron signal from SNM or WGPu and the FLI ProLine camera produced images at an extremely slow read-out speed. Further, a short study showed the read noise of the FLI ProLine camera was ten-fold the read noise of the EMCCD camera. Finally, the EMCCD camera is insensitive to Residual Burn-Ins. This is a common concern for the DMTPC collaboration, presenting a possible background signal which produces a low energy, short track after image blurring and analysis. As a further method to prevent reading out an RBI as actual data is to cut at a minimal range. The EMCCD camera is read-out through an Andor custom cable through a PCI card installed on a computer built into the detector.

The choice of lens is a complicated decision that is camera and detector specific. As a result of the distance between the ampliciation region and the camera, the Schneider 25mm f/0.95 lens was chosen when imaging the full anode, providing the 1.3 centimeter by 1.3 centimeter 1MP EMCCD chip a view of the entire amplication plane. The lens actually captures more than just the amplification plane, wasting some of the EMCCD chip, but the more optimal 28 mm lens is not produced with as low an f/#, significantly reducing the effective diameter of the lens. The electron avalanche that occurs along the ionization track (after drifted to the amplification region) produces light isotropically. Therefore, the signal is an extremely low-light track, requiring the lens to capture as much of this light as possible. The effective diameter of a lens is described by the focal length divided by the F-number. The 28mm lens options provided F-numbers down to 1.8, resulting in an effective diameter of 15.6 mm. This lens produced a signal that was only marginally above the camera's

pixel-to-pixel noise level. However, the Schneider lens, with an effective diameter of 26.3 mm, increased the captured light by more than three times. Further, the tracks are shorter on the EMCCD chip using the Schneider lens than with the 28mm lens options, resulting in more photons per pixel, and further increasing the signal-to-noise ratio. The expected pixel-to-mm conversion is approximately three pixels per milimeter. Due to diffusion, the lower bound for energy cuts will be 100keV, which has an expected 3mm track length. The decrease in spatial resolution for the 25mm focal-length lens will not drive the resolution of this detector.

Additionally, the direct energy deposition from cosmic muons into the silicon of the pixel-chip array may result in a false signal. The cosmic muon interactions were studied to determine the characteristics of the interaction. The central pixels receiving the energy deposition from the muon saturate the pixel and pixels in the direction of read-out are progressively less energized, leaving a track in the range of tens of pixels. This systematic background would otherwise produce a signal in perfect agreement with the row read-out direction due to the characteristics of interaction. These tracks are easily cut from data by excluding any track discovered by the imaging software with a maximum pixel above 10,000 ADU, which is three orders of magnitude above a typical nuclear recoil maximum pixel and only one-fifth of the ADU count for a saturated pixel.

The electromagnetic ampflication, known as EMGain, process involves shifting each row to a read-out array of pixels, which are passed through an entirely separate array of voltage-biased silicon pixels. In each pixel step, there exists a probability that each signal electron is multiplied to two electrons. At an EM Gain of 300, a binomial distribution with normalization of 0.03 was produced in a short collaboration for an in-class experiment studying the characterization of the cosmic muon interactions with CCD pixel arrays[36]. This gives the camera the ability to completely overtake the noise in the conventional pre-amplifier, but places an upperlimit on how high

the EMGain is operated. There is a non-negligible probability that an electron-hole will form in each pixel, known as dark noise. This electron-hole will be amplified as a true photon signal in the EMGain process. This noise increases the longer the exposure time, with each pixel having a higher probability of a random electron-hole forming. Further, as each row is shifted, there is an additional probability of creating an electron-hole in the process. This noise is known as clock-induced charge and becomes a factor when the vertical row shifts are conducted slowly and the horizontal read-out is conducted quickly. The dark noise and clock-induced charge become the dominant source of pixel-to-pixel noise. Therefore, the signal strength sought was such that it would reside well above the source of pixel-to-pixel noise, resulting in an accurate depiction of the track length and total energy. The primary two considerations for seeking such a signal to noise ratio are the anode gain and the lens' effective aperture, discussed earlier.

Using the DMTPC software, the software brings all the voltages down to zero volts potential difference from ground and exposes the camera for 100 seconds of dark frames. The average of these 100 dark images create a bias frame, which is subtracted from every image prior to image analysis. Towards the end of this experiment, the Data Acquisition (DAQ) software was adjusted to operate in a near realtime environment. The program conducts a single bias frame scan at the beginning of a 20,000 second run. After the bias frame is conducted, the software produces a single image file in preparation for image analysis and produces a 500 image raw file for data backup. The single image file is converted into the proper analysis file format and pushed through the DM-TPC image analysis software. The analysed single image file is held until the Graphic User Interface opens the file, pulls pertinent information, and then deletes the temporary single-image, analyzed file.

2.4 Supporting Hardware and Software

The most important aspect of the supporting hardware is the remote power control. By design, this chamber was constructed to demonstrate a remotely operated SNM/WGP detector, where the detector itself could principally reside anywhere with sky coverage or direct internet access and the monitoring system can exist through a remote monitor system. With a compressed gas cylinder permanently connected to the detector, the remote operator would be capable of cycling the fill gas once per week. This is accomplished through the power supply to two valves installed on the gas-in and gas-out valves, connected to a compressed gas bottle and the vacuum pump, respectively and has been demonstrated extensively through a typical LAN network system, over the world wide web, and most recently (and only briefly) over a 4G modem. The remote power control, or Synaccess, provides eight power controls, each providing power to the components of the detector[37]. Two 120VAC computer fans were installed to provide cooling air to the EMCCD camera.

The GUI was constructed specifically for characterization testing at Oak Ridge National Laboratory (ORNL) and is depicted in Fig. 2-7. The testing involved short runs with a wide range of neutron and gamma sources and detector operators who are not familiar with Linux or ROOT data analysis software. Given these circumstances, a GUI framework was constructed to provide real-time feedback on the detector's performance. The GUI provided a small print out of the camera's image, spark rate notification, source detection notification, and four separate instances of data presentation. The first plot depicts a simple one-dimensional histogram for the number of events in each 10-degree phi window. The second depicts a two-dimensional histogram that plots the energy of the track as a function of direction, or ϕ. The third presents the source detection direction as a function of time, in an effort to provide some feedback for a slow moving source. The last plot, centered on the GUI, presents the detected source direction, which is the peak of a gaussian fit on the phi one

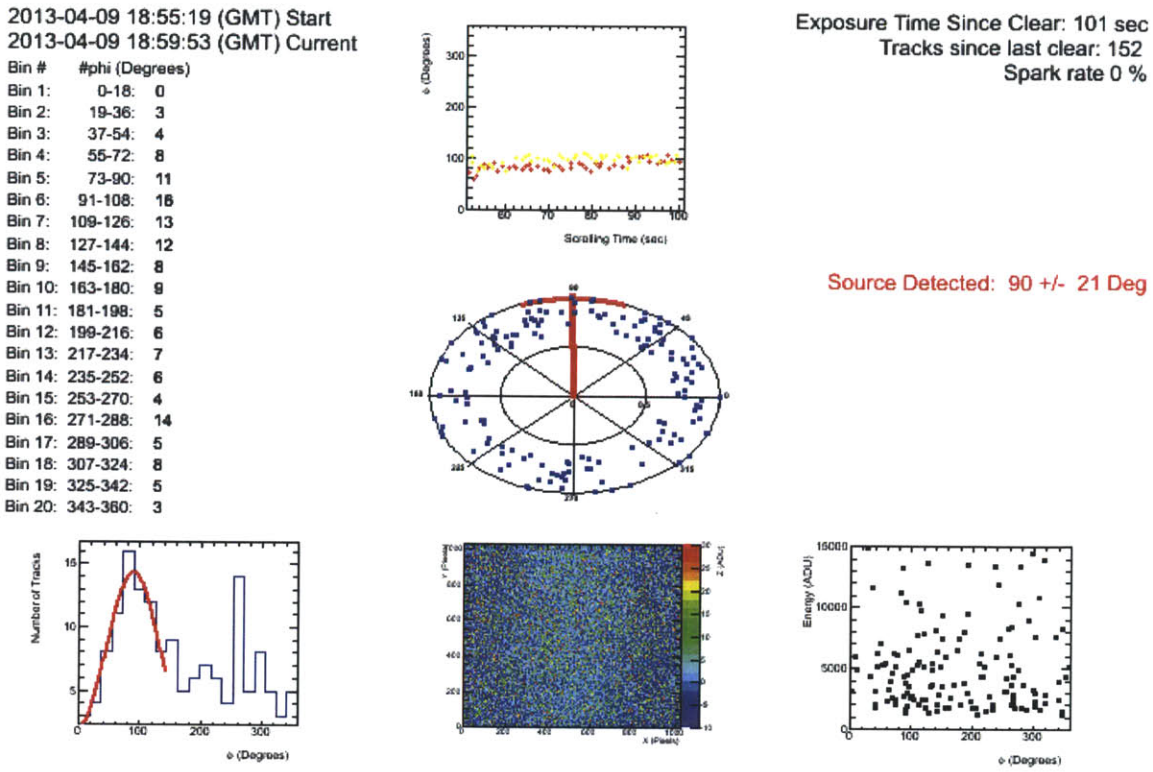

Figure 2-7: An example of the Graphic User Interface after 101 seconds with a 200,000 neutrons/second ^{252}Cf source at 2 meters.

dimensional histogram.

Six months prior to taking the detector to testing at ORNL, the detector was rotated to place the anode/amplification plane parallel to the earth's surface. The testing uses sources that move in and around the same plane as the detector, indicating the need for a better directional resolution in a plane parallel to the earth's surface. The final detector configuration prior to test is presented in Figures 2.4 and 2.4.

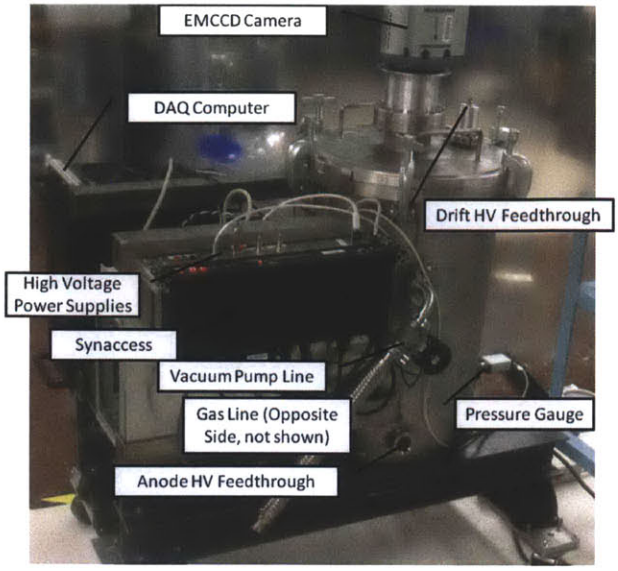

Figure 2-8: The detector configuration after the chamber was rotated and placed with amplification region parallel to the earth's surface.

Figure 2-9: The final detector configuration prior to characterization testing at ORNL.

Chapter 3

Experiment

The release of atomic energy has not created a new problem. It has merely made more urgent the necessity of solving an existing one.

A. Einstein[24]

The primary purpose of this experiment was to investigate the feasibility of using the technology and software developed by the Dark Matter Time Projection Chamber to provide directional detection of SNM, specifically WGP. The method of testing involved multiple short studies to determine the optimal operational settings and orientation of the detector, followed by several extended runs using two neutron sources with different energy spectrums. Further, a simulation using Geant4 was conducted to test the efficiency of the detector and produce theoretical limits for future uses.

3.1 Operational Studies

The vessel purchased for this experiment was capable of achieving two bar of absolute pressure and 0.5 Torr of near vacuum. The procedures to pump down the chamber to near vacuum prior to filling with proper fill gas were limited to the capabilities of the pressure vessel. Although the DMTPC collaboration pumps down using a turbo

pump to 10-5 torr, this detector showed no obvious degraded performance pumping to only .5 Torr and operating at 1.5 bar. Initially, all studies focused on using 100% tetraflouromethane, or CF4, to test the compatibility of the DMTPC collaboration's software with the new experimental components. The EMCCD camera and the high voltage power supplies were both new additions to the DMTPC software. The early tests further provided a baseline of operation, providing insight to the operation of the EMCCD camera and the possible gain values. After the initial baseline characterization, a diffusion study was conducted to understand the degradation of directional signal as a function of drift distance for the ionization track. Using this information, these baseline studies were conducted with similar anode and cathode settings at one atmosphere. Finally, the detector was operated at an optimal setting of 1.5 atmosphere absolute pressure with anode and cathode settings adjusted to account for the different pressure. Using this optimized setup, the camera and lens combination was tested to find the optimal combination to image the entire anode ampliction plane.

3.1.1 Baseline Characterization

For the first detailed characterization study of this detector, a neutron source with a 26,000 neutrons per second intensity was placed next to the detector for an extended period of time. The source, which was later used in extensive studies, is known as a Troxler gauge and is traditionally used as a ground-water detection system, scanning for neutrons on the surface after lowering this neutron source into the ground[38]. The modern gauges use a 40 milicuries (mCi) ^{241}Am source on Be target, while the source used in this experiment had 10 mCi. The isotope ^{241}Am is in immediate contact with Berylium, with alpha-decay particles causing fission in the Berylium, with corresponding neutrons. According to experimental studies re-produced in *Radiation Detection and Measurement*[39], 70 neutrons are produced isotropically for every one million ^{241}Am decays, resulting in an approximate source intensity of 25,900 neu-

trons/second. Further, this source maintains an energy spectrum as depicted below, with several peaks at energy ranges of 1 MeV:

Although this source sits slightly higher than the energy range better suited for this detector, the AmBe neutron source proved a robust source with which to tote around and calobrate the detector. This source was initially used to collect data for carbon recoils in 86.9 Torr CF4 over a period of 4,000 seconds of actual exposure varied between positions along the axis of drift. The raw data is plotted for reference in Fig. 3-1. For each data point, the energy is the total Analog-to-Digital-Units above the average biasframe values. This provides the signal above the noise of the camera and can be used to scalc ΛDU to keV. The range is a projection of the total ionization track range onto the X-Y anode-amplification plane. The range-energy plot is scaled to fit the Stopping and Range of Ions in Matter (SRIM) experimental data curves. For every 100 Analog-to-Digital-Units (ADUs) along the x-axis, the data is placed in a one-dimensional histogram and fitted with a gaussian curve. The gaus fit returns a peak and sigma, which is used to scale the best fit data points to the SRIM curve. To account for the X-Y projection of the range onto the anode plane, the best-fit data points are fit to one sigma below the SRIM curve using a numerical minimization routine.

Each data point is compared with the SRIM curve at the similar position using χ^2 as the statistical significance:

$$\chi^2 = \frac{(R_{pixels} + \sigma_{Gausfit} - \alpha * R_{SRIM_m m})^2}{\sigma_{Gausfit}} \tag{3.1}$$

where R_{SRIM} is the value of the SRIM curve evaluated at $E_{keV} = \beta * E_{ADU}$. The α and β scaling factors are minimized using the numerical minimizer from ROOT. The α scaling factor is constrained due to the geometry of the setup. Using typical optics geometrical calculations, each pixel is $13\mu m$, with a focal length of $55mm$ and distance between lens and anode of $67cm$. Using Formula 3.2:

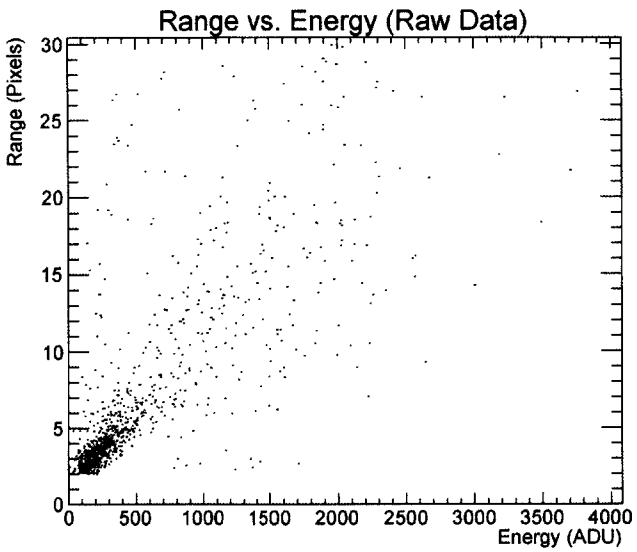

Figure 3-1: Range Versus Energy with Unscaled Data Points. Each data point corresponds to a single track after edge, maximum pixel, minimum range, and minimum energy cuts are applied. This data was taken over a total exposure time of 11 hours or 26 hours of actual detector operation.

$$\frac{h}{H} = \frac{f}{l} \tag{3.2}$$

the pixel to millimeter scaling factor is 6.3 pixels/mm. Using this to constrain α of the χ^2 fit, the energy scaling factor β is minimized to 19 ADU/keV. This value is compared with a rough calibration using an alpha source. The alpha decay products from a small Americium produce ionization tracks. Recoiling nucleii exhibit a characteristic bragg peak, where the largest differential energy deposition occurs. The bragg peak for alpha particles occur at approximately 1.5 MeV. The peak energy in the bragg peak is compared with the peak ionization of the SRIM, yielding an energy scaling factor of roughly 20 ADU/keV. The former is a more thorough method of calibrating the total conversion from recoil energy to ADU and will be the method used for the extent of this experiment. Further, the statistics in this early test were limited due to the low pressure gas yielding a much smaller total cross section.

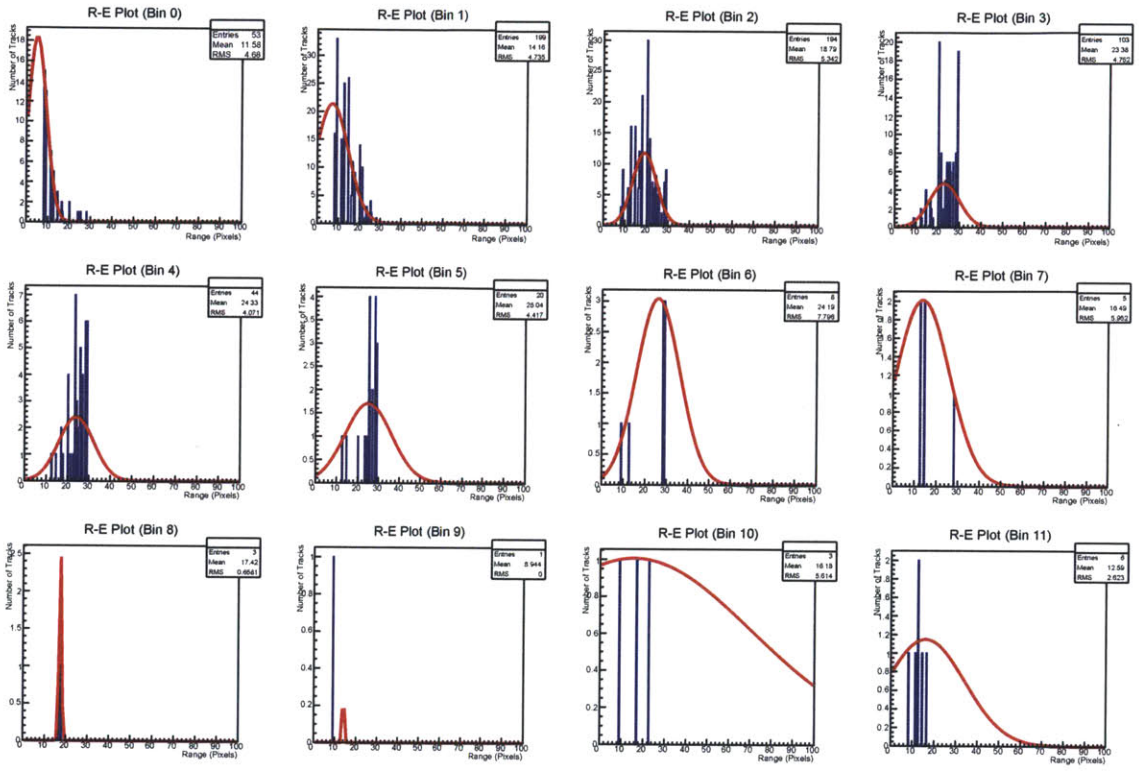

Figure 3-2: Twelve histograms depicting the gaussian fits to each energy slice of the range-energy plot in Fig. 3-1. Each fitted data point is used in a χ^2 minimization process to produce a rough keV-ADU energy conversion factor. Bin Nine appears to mix the peak, but the peak is actually a systematic noise problem with software written to not fit to this peak. This artifact can be seen in other bins with less prominence.

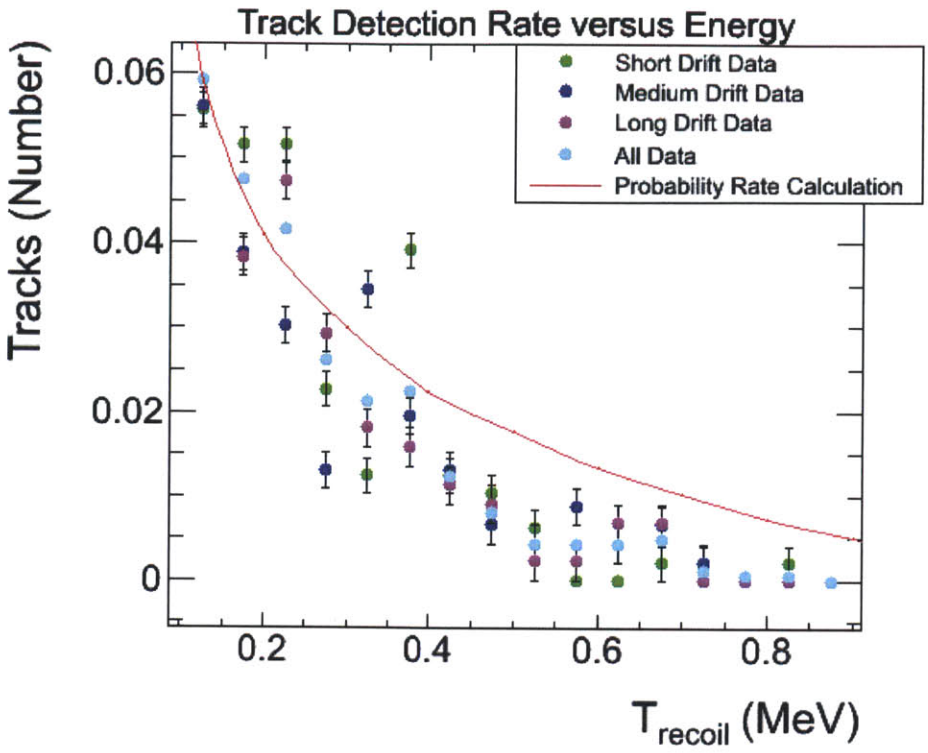

Figure 3-3: The rate of nuclear recoil detected by the DMTPC image analysis software plotted for each drift distance, plotted as a total rate for all data points, and plotted against a probability calculation curve using the energy spectrum of an AmBe neutron source and cross sections of target nucleii[40, 22]. The recoil rates were binned into 100keV bins and normalized by dividing by bin-width to return an appropriate rate. The errors are plotted as typical Poisson error bars, derived from the number of data points in each bin.

To further constrain the energy scaling factor calibration, a probability rate-based calculation was conducted. The data tables for the cross section versus energy of each nucleus, ^{12}C and ^{19}F, were uploaded from ENDF into ROOT and used in conjuction with the energy spectrum for an Americium-Berilium neutron source[40]. More detailed plots are presented in Appendix A describing the calculation to arrive at a nuclear recoil rate as a function of nuclear recoil energy. The result is presented in Fig. 3-3.

As seen in Fig. 3-3, the rate for each drift distance does not decrease appreciably between the different recoil energy ranges. The data generally agrees with the proba-

bility based calculation, given the low statistics. As a result of this baseline study, the detector seemed to be in appropriate working order and these methods of calibrating the energy scaling factor were carried further to future tests.

3.1.2 Helium-CF4 Gas Mixtures

Previous studies presented by Ahlen *et. al.* indicate using the same technology while CF4 provides the gas gain and a bath of Helium-4 provides the primary target medium [23]. In this experiment, the collaboration conducted testing with 80 Torr CF4 alone, as well as with 80 Torr CF4 in a bath of 560 Torr ^{4}He. The studies show the increase in nuclear recoil rate due to the increased number of nuclei resulting from the ^{4}He bath. With the CF4 operating as the amplification gas, the voltage settings are closely related to the CF4 Paschen curve limits. Several short baseline runs were conducted to find the optimal gain settings at 1.5 atmosphere, the optimal pressure setting due to chamber construction and hardware availability. After determining the optimal gain settings, multiple runs were conducted with the AmBe neutron source at three positions along the drift length. At each position, the detector was operated for 10,000 seconds of exposure, with an accompanying 10,000 seconds of exposure to background only. The raw data plotted as a function of range versus energy with source present and with background only is depicted in Fig 3-5, with the former plot nested behind the expected SRIM curve.

The range calibration was carried forward from the previous testing since the lens, camera, and geometrical setup was identical. This allowed the same routine to calibrate the energy conversion factor for the 1120 Torr gas mixture. With the same amount of total exposure time for each position of the AmBe source, the total number of data points were much higher and resulted in a better fit to data. These fits are presented in Fig. 3-4 and 3-5. With the proper scaling factors, the probability-based rate calculation was conducted and is presented in Figures 3-6 and 3-7. The

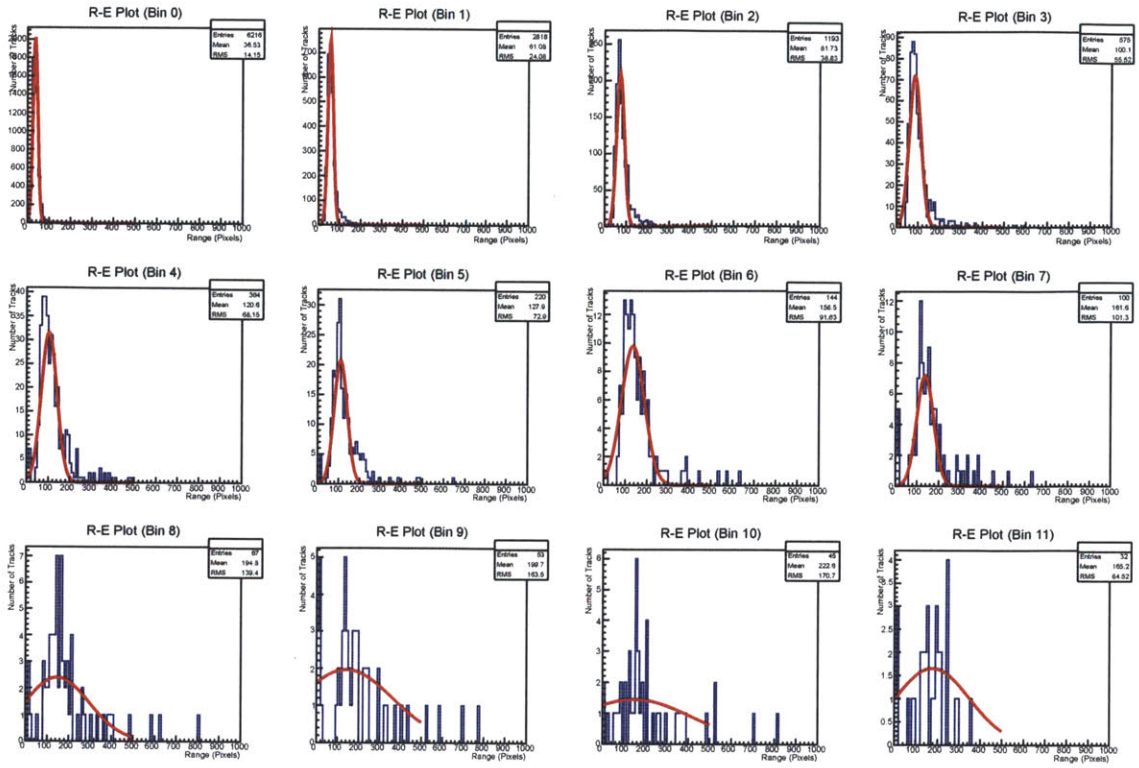

Figure 3-4: The cross section of the range-energy plot depicted for each bin with a Gaussian fit for 1120 Torr 94% He: 6% CF4. This data is used to fit to the SRIM curve for a range-energy scaling factor calibration.

difference between the neutron source data points and the expected rate curve at low energies are attributed to large thermal fluctuations in the EMCCD chip, amplified as low energy tracks. This can be significantly reduced by increasing the number of photons arriving at each pixel through a lower f-number lens, increasing the focal length of the lens, or placing the camera closer to the amplification plane (with the latter two effectively accomplishing the same thing, a larger effective diameter). The background rate was computed using EXPACS, with an expectation curve based on no surroundings.

The detector took all data in a radiation vault, surrounded on all sides by a meter of concrete, significantly reducing the number of background neutron tracks. The attenuation of a neutron signal can be estimated by Eqn. 3.3, where $I(x)$ and I_0 are the intensities after x-meters and initially respectively[41].

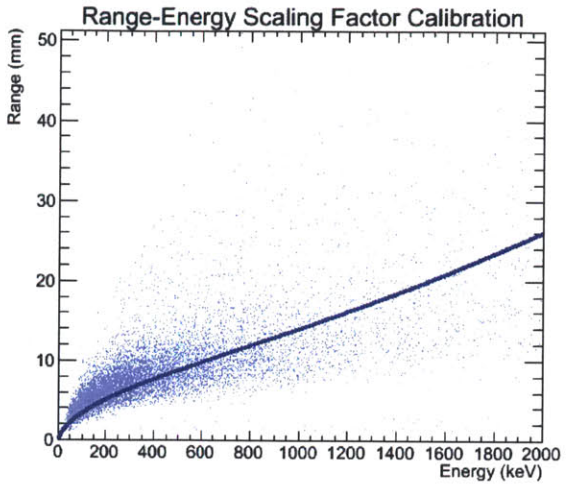

Figure 3-5: The range versus energy data points plotted with the Gaussian fit points and SRIM predicted curve. The vertical error bars on the Gaussian fit points are the sigma from the Gaussian fit.

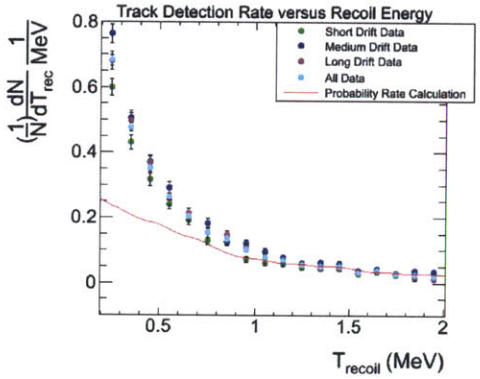

Figure 3-6: The total rate as a function of recoil energy for 1120 Torr 93.75% Helium and 6.25% CF4.

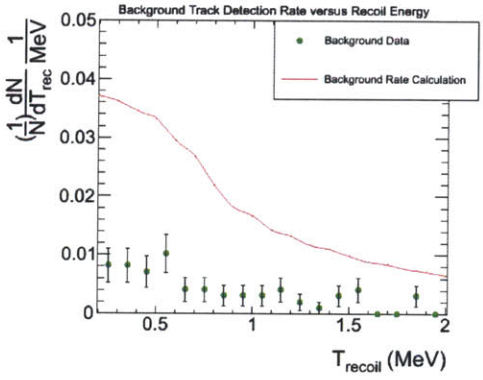

Figure 3-7: The total background rate as a function of recoil energy for 1120 Torr 93.75% Helium and 6.25% CF4 and no neutron source present.

$$I(x) = I_o e^{-N\sigma_t x} \tag{3.3}$$

The number of nucleii, N and the total neutron cross section, σ_t are estimated in the macroscopic case by Eqn. 3.4,

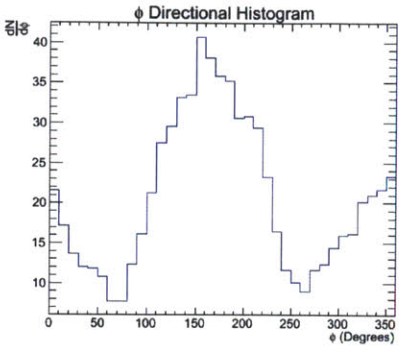

Figure 3-8: The raw phi data plotted in a 1D histogram with 10 degree bins.

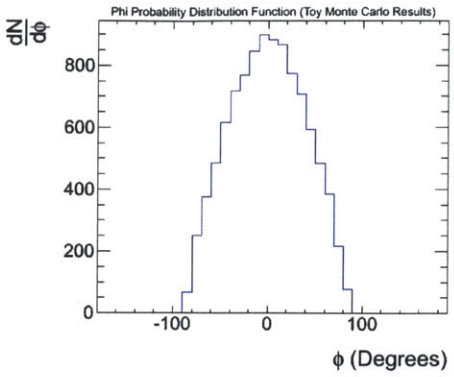

Figure 3-9: Directional histogram produced from a parameterized monte carlo simulation to provide the expected shape from a point source at 30cm with zero background events.The overlaid curve is the typical expected two-body kinematics cosine-squared curve.

$$\Sigma = \frac{\rho N_a}{M}(n_1\sigma_1 + n_2\sigma_2 + n_3\sigma_3 + ...) \tag{3.4}$$

where N_a is Avogadro's number, M is the molecular weight, ρ the density, and n_i the number of nucleii in each molecule. In order to compare a general understanding of the attenuation, the meter of concrete surrounding the vault was taken to be typical Portland cement, with "67% CaO, 22% SiO_2, 5% Al_2O_3, and 3% Fe_2O_3[42]. The attenuation is equal to 4E-12. Therefore, the tracks detected in the source free running of the detector can also be attributed to thermal flucuations of the EMCCD chip and the chip cooling capabilities.

After calibrating the signal to appropriate recoil energies and recoil ranges and checking detection rates, the data was analyzed for directional sensitivity. The track information recreated by the DMTPC image analysis software includes the phi direction, defined as the counterclockwise rotation from the positive x-axis. A first look at the signal from all alpha-particle recoils over 3,000 seconds of exposure show a significant peak just under zero degrees. This data is presented in Fig 3-13.

In order to represent this data more effectively, two methods of data fitting were conducted. As will be discussed earlier, the real-time run environment was written to use a simple Gaussian peak fitting procedure, where half of the standard deviation was returned as the uncertainty window. This was chosen directly with the ORNL technicians to be an appropriate feedback level. Any larger of a window and the uncertainty for a strong signal overwhelmed the information and any smaller gave a false sense of certainty. This section focuses on a more detailed approach which may be incorporated in future phases of this work using dedicated micro-processors. In order to compare this signal with an expected signal, a parameterized monte carlo was conducted to produced the cosine-squared shape expected through classical two-body kinematics. Ignoring all second order effects and simply computing the recoil direction from neutron emitted by a point source at 30 cm, the expected shape of the curve is depicted in Fig. 3-9.

An interesting observation from the parameterized monte carlo is the width of the curve at the half-max position. A uni-directional beam of neutrons would return a probability distribution function almost exactly fit to the cosine-squared distribution, but neutrons from a nearby point source increased the width of the curve, as depicted in the cartoon diagram and associated PDF plots in Figures 3-10 and 3-11. This feature could be used in the future to test for source distance inside of some critical range. In other words, beyond a certain distance this method will not be effective, but inside this critical distance the detector should be able to predict a rough estimate of the distance to a point source.

Using the normalized and parameterized monte carlo phi distribution histogram as a probability distribution function, the phi histogram was cycled through ten-degree bins and the log-likelihood was computed at each interval. The p.d.f. was evaluated for each bin of the phi-data directional histogram with the free parameter, θ, being the start bin of the window, which corresponds directly to the direction estimate by

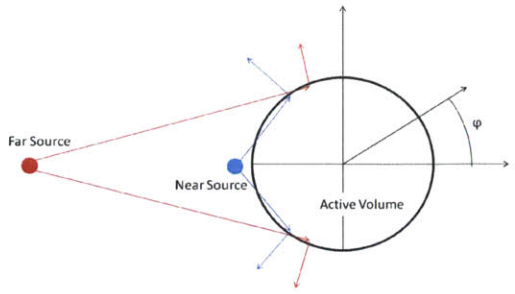

Figure 3-10: This figure depicts the reason for varying phi probability distribution functions resulting from different source distances.

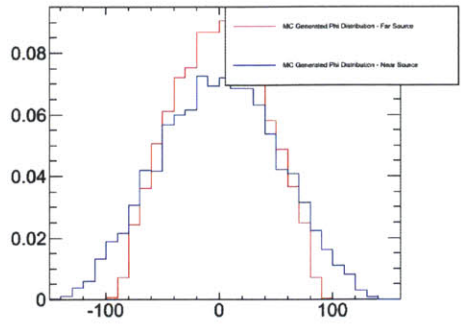

Figure 3-11: This plot shows a randomly generated, normalized PDF for sources at five centimeters and one meter

$\theta = \pi - \phi$. This value corresponds to the ten-degree bins. The log of the likelihood function, reproduced below in Eqn. 3.5,

$$L(\theta) = \prod_{i=1}^{N} f(x_i; \theta) \tag{3.5}$$

is added for each bin and plotted as a function of the total log-likelihood [43]. The maximum of this function is the maximum likelihood for the estimator θ and returns the estimated direction of the source. To reproduce uncertainty, one standard deviation, s, was used in the form of Eqn. 3.6 [43]:

$$lnL(\theta') = lnL_{max} - s^2/2. \tag{3.6}$$

which corresponds to 68.2% of the maximum likelihood data points existing inside of this value. Simply, a strong signal will have a much narrower Gaussian returned for the plot of the log-likelihood. In Fig. 3-12, the log-likelihood for all possible values of θ is presented. This plot corresponds to a neutron source at 166 $\pm$ 7 degrees. This signal is plotted in a polar graph overlaid on an image of the specific setup for this run in Fig. 3-13.

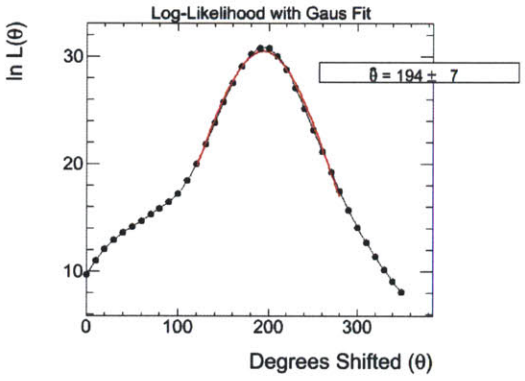

Figure 3-12: The plot of total log-likelihood sums as a function of start bin, θ.

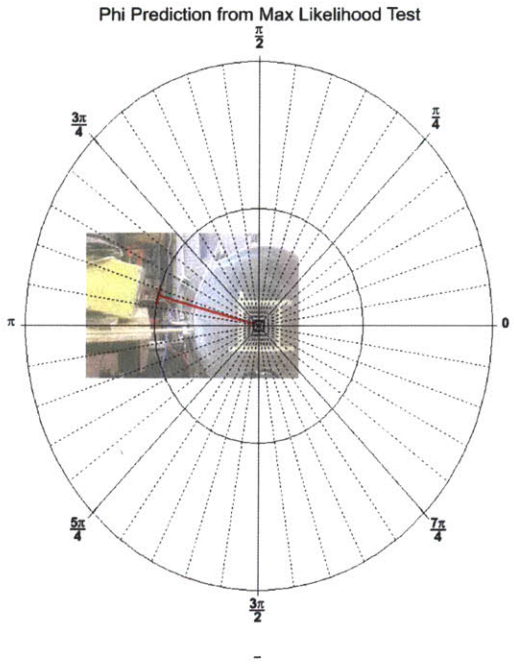

Figure 3-13: Phi Estimator Returned from Maximum Likelihood test with angular errors represented at the end of the directional line. These error bars are computer with one sigma significance. The yellow box is the Troxler gauge with the source contained on the far right side and central 1/3 of the yellow container.

The image depicted beneath the polar graph is a mirror image of the actual setup due to the camera viewing angle. The angle returned for the maximum likelihood estimator is seen from the detector's EMCCD camera reference frame, which is opposite the direction of the photographer's reference frame. The yellow box is the troxler gauge which houses the 10 mCi AmBe source, with an effective neutron intensity of 25,900 neutrons/second [39]. As seen in the polar graph, the maximum likelihood fit returns a direction in strong agreement with the source location, and the error of the fit is approximately the width of the source in the box. The parameterized monte carlo probability distribution function was constructed using a point source, while the size of any source obviously has some finite thickness. Neutrons during this data run would have been emitted from anywhere within 75% the width of the uncertainty bars on this directional signal.

3.1.3 Diffusion Study

In keeping with the primary focus on this experiment to determine the feasability of providing a directional signal from fast neutrons emitted from WGP, a brief diffusion study was conducted to determine the loss in directionality at lower energy levels and long drift distances. As depicted in Fig 2-3, the expected longitudinal and transverse diffusion for a 48 cm drift is 2.6 mm and 2.9 mm respectively. Using the SRIM tables to extrapolate projected ranges for 1.5 atmosphere of 94% He and 6% CF4, energies below roughly 50keV will equate to near circular tracks after 48cm of drift and diffusion[44]. Three 10,000 second runs were conducted. For run one, the source position was slightly inside of the anode amplification plane, with runs two and three in the middle of the drift distance and immediately inside the cathode. The source was colimated to make a predominant signal at each drift position. In Fig 3-14, the ratio of longitudinal to transverse standard deviations is plotted as a function of energy (binned in energies of 50keV).

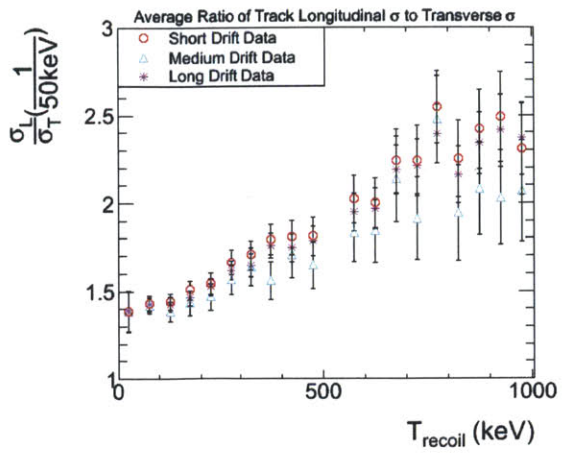

Figure 3-14: The ratio of longitudinal to transverse standard deviation as a function of recoil energy

The results of this agree with the diffusion and SRIM expectation curves[44]. Energies below approximately 50keV are approaching a circular track where the transverse and longitudinal standard deviations are approximately equal. The cuts used for the extent of this experiment varied between 100 and 200 keV, which agree with the expected loss of directional signal below 100keV.

3.1.4 Full Anode Imaging

The image processing system was tested to provide optimal signal to noise ratio while imaging the full anode, a copper-clad G10 circle with a 12.25" electrically isolated plane in the center serving as the anode. There are three variables which can be adjusted to image a wider area: 1) Increase CCD chip size, 2) Decrease focal length of the lens, 3) Increase distance between camera and anode. The first option poses the most optimal, but resulted in less than optimal running conditions. As discussed, the CCD chip was much larger, with 3056X3056 pixels each $12\mu m$ wide. Making no other changes to the detector, the 55mm lens provided an image plane of 45cmX45cm. However, the CCD camera proved a much higher noise level and slower readout. The average time for each image was approximately four seconds,

which aligned appropriately with the manufacturer's expected read-out speed. This read-out speed was also at optimal conditions, while the one second read-out of the Andor EMCCD was sub-optimal, leaving the ability to switch to frame-transfer for future phases. Further, the pixel-to-pixel noise had an RMS of 19ADU, versus an EMCCD pixel noise RMS of 3ADU (at 100 EMGain, an option not available to the CCD camera). As a result of these variables, the CCD camera was abandoned early in the testing and method 2) was approached. Initially, a 28mm lens with f/# of 1.8 was installed, and the EMGain was operated at 100, versus previous runs of 10 EMGain. This setup provided tracks marginally above the camera pixel-to-pixel noise. The final lens chosen was a Schneider 25mm, f/# 0.95. This provided an effective diameter for the lens of 27.4mm, versus the 28mm lens of original effective diameter of 46mm. This change resulted in a 64% reduction in solid-angle acceptance of scintillation photons from the amplification plane. To account for the drop in acceptance, the EM Gain was ajusted to 100, versus the previous setting of 10. With these settings, the ionization tracks appeared as clear tracks above the 3ADU RMS pixel noise.

With this set-up, 25,000 seconds of exposure were taken with the AmBe source next to the chamber to determine if the rate agrees with the probability-based rate calculation. The range-energy data points are plotted with the expected SRIM curve overlaid in Fig. 3-15. Using this data, the track detection rate is compared to the expected rate in the adjacent figure, Fig 3-16.

As seen, the track detection rates generally agree with the expected rates, understanding low energy noise can be attributed to large thermal fluctuations of the EM-CCD pixels, as seen in the partial anode imaging data. With the track detection rates in agreement with the expectation rates, the directionality signal was tested with the same Max-Likelihood test from the partial anode imaging. The same parameterized Monte Carlo probability distribution function was used against the one-dimensional

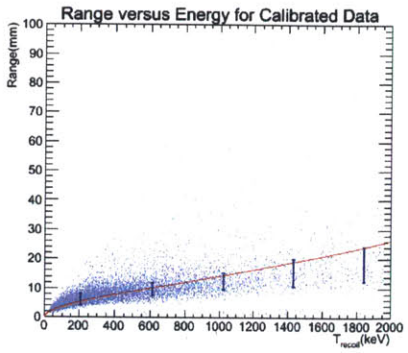

Figure 3-15: The range-energy plot for data surviving cuts for the full anode imaging. The range for data points is a projected range onto the amplification region while the SRIM data curve is full range. The energy-binned range fits are plotted additionally to view the level of agreement between SRIM and data points.

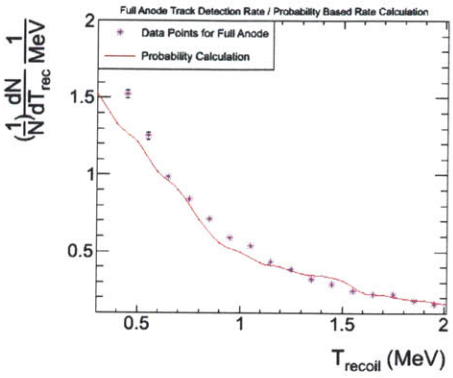

Figure 3-16: Track detection rates from full anode imaging compared with expected rates.

phi histogram to test for an approprate signal. The one-dimensional phi histogram is reproduced in Fig. 3-17, with the log-likelihood plotted in the adjacent figure, Fig. 3-18. As can be seen in these two figures, there exists an almost equally strong signal at exactly 180 degrees apart. This signal is predominantly attributed to the significant decrease in head-tail accuracy at energies which place the bragg-peak directly in the middle of the track. The bragg peak for recoiling alpha particles is re-produced from the SRIM data curves in Fig. 3-19. As discussed earlier, the bragg peak for recoiling alpha particles occurs at approximately 1 MeV, significantly degrading head-tail reconstruction efficiency at energies up to approximately 3 MeV (understanding the peak occurs in a projection, smearing the location of the peak and thereby degrading the efficiency above just 2 MeV). In order to partially compensate for this effect, phi's produced from tracks with energies above approximately 3 MeV were reversed, as the head-tail assymetry above this energy was reversed.

Again, using the one sigma deviation to produce uncertainty on the directional signal, the polar graph is printed directly on top of the image for this run, where,

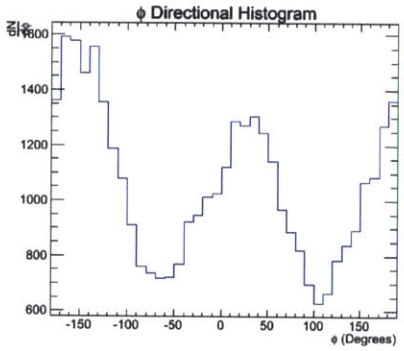

Figure 3-17: A one-dimensional histogram showing the number of tracks for each 10 degree bin.

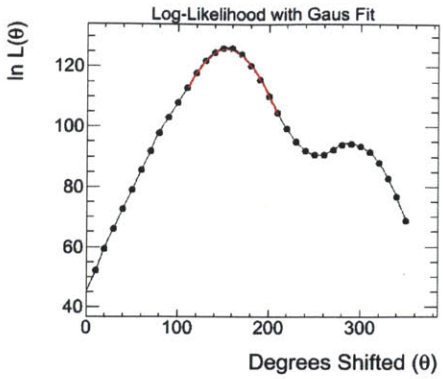

Figure 3-18: A log-likelihood graph depicting the data fit to a parameterized monte carlo probability distribution function

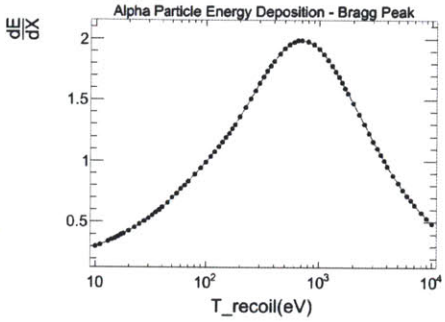

Figure 3-19: The bragg-peak depicted in the energy deposition as a function of the recoiling energy

again, the 10 mCi AmBe source is housed in the yellow box in Fig. 3-20.

3.1.5 Geant4 Simulation

A Geant4 simulation was written in order to verify the rates produced from the probability-based rate calculation, as well as from the full anode imaging data. Geant4 is a "software toolkit for the simulation of the passage of particles through matter" [45, 46]. Within the framework of Geant4, the main detector components were recreated to provide a broad understanding of the nuclear recoil rate from an AmBe source approximately 5 cm from the active volume of the detector, as in the final data set. The simulated field cage is depicted in Fig. 3-21. As shown, only the major

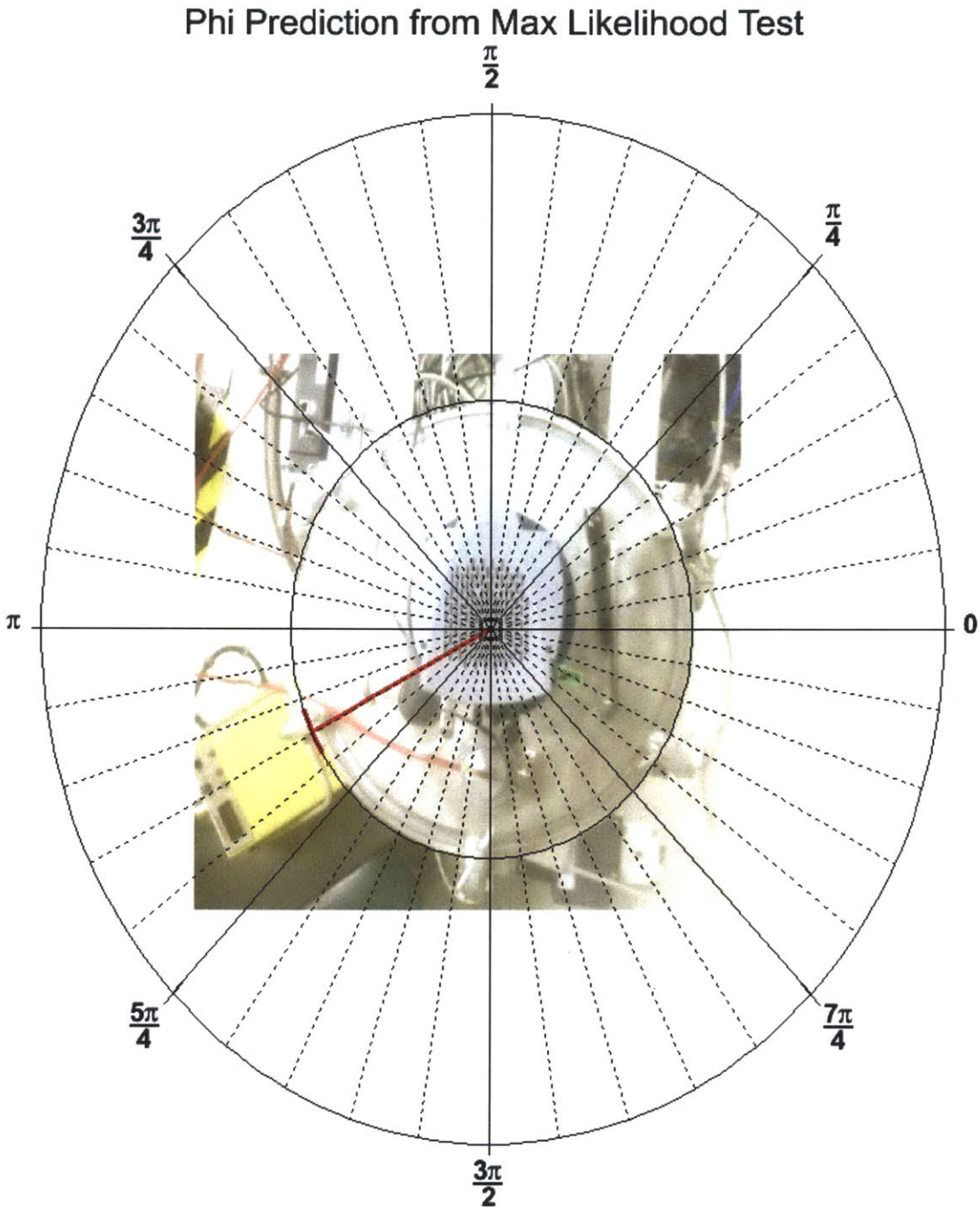

Figure 3-20: The Directional Signal for a 10mCi AmBe Neutron Source with Full Anode Imaging

components were considered in this simulation to give a broad understanding of the recoil track detection rates. The chamber walls (although not drawn in the figure)

and the copper rings were included in the simulation, but not the ports or plastic rods, which would effect the total rate minimally.

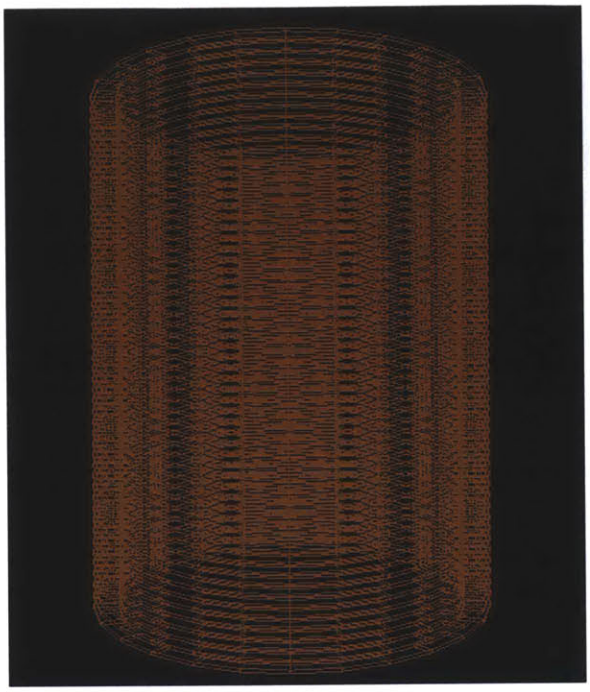

Figure 3-21: The simulated field cage rings filled with the primary sensitive volume fill gas at 1.5 atmosphere 93.75% He and 6.25% CF_4, built within the framework of Geant4 Simulation software.

A simulation of neutrons with the appropriate AmBe energy spectrum was conducted for an equivalent 4,200 seconds to provide a simulated energy-dependent rate curve. The results of this simulation are plotted against the results of the probability rate calculation, as well as the data from the full anode imaging data points in Fig. 3-22.

3.1.6 Head-Tail Assymetry

The final study completed during this phase of the experiment was to determine the accuracy of determining the head versus the tail of the track with a large data set. The DMTPC collaboration only images carbon or flourine recoils, whose bragg peak occurs at much higher energies. However, for a recoiling alpha particle, the bragg

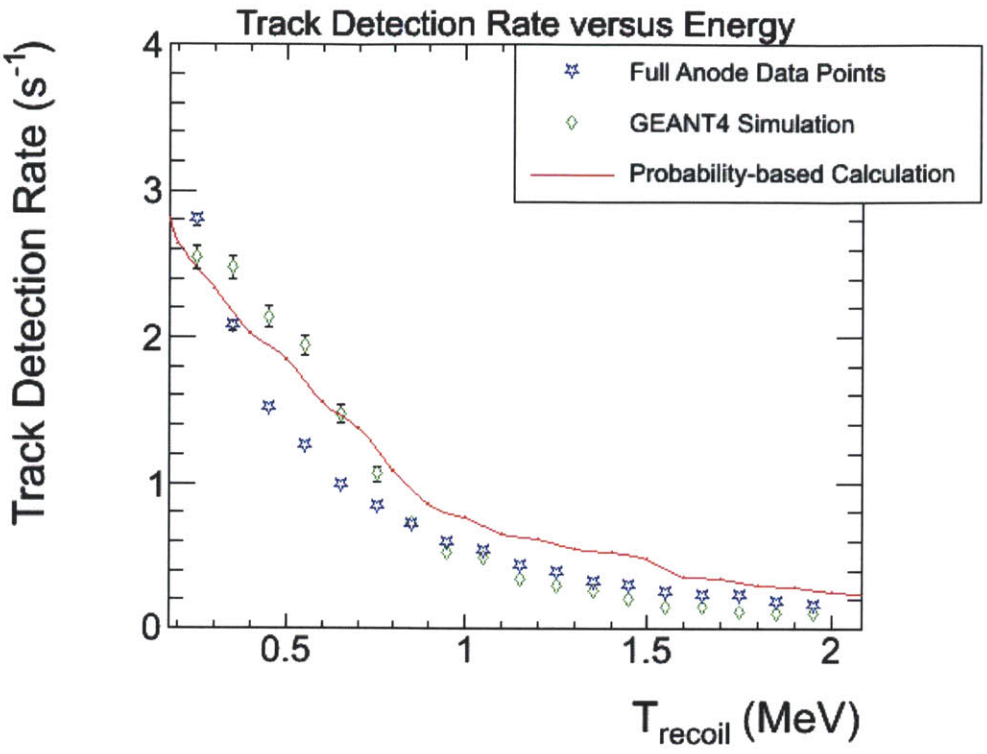

Figure 3-22: The Geant4 simulated rate plotted against the probability-based rate calculation curve as well as the actual data points from the full anode imaging run.

peak occurs at approximately 1.5 MeV [44]. Therefore, depending on the inclination of the track, the software will be guessing with 50% accuracy at energies up to 3 MeV, or higher. Therefore, at energies below this range, the head-tail assymetry will be somewhere around 50%. However, at much higher energies, the head-tail determination will be much more accurate due to a much longer track and software that was tailored for Helium operations to reverse the signal at energies above 3 MeV. Depicted in Fig. 3-23, the full anode data is binned by 200keV bins from zero to 8 MeV and the head(n_h)-tail(n_t) assymetry, $\frac{n_h - n_t}{n_h + n_t}$, is computed.

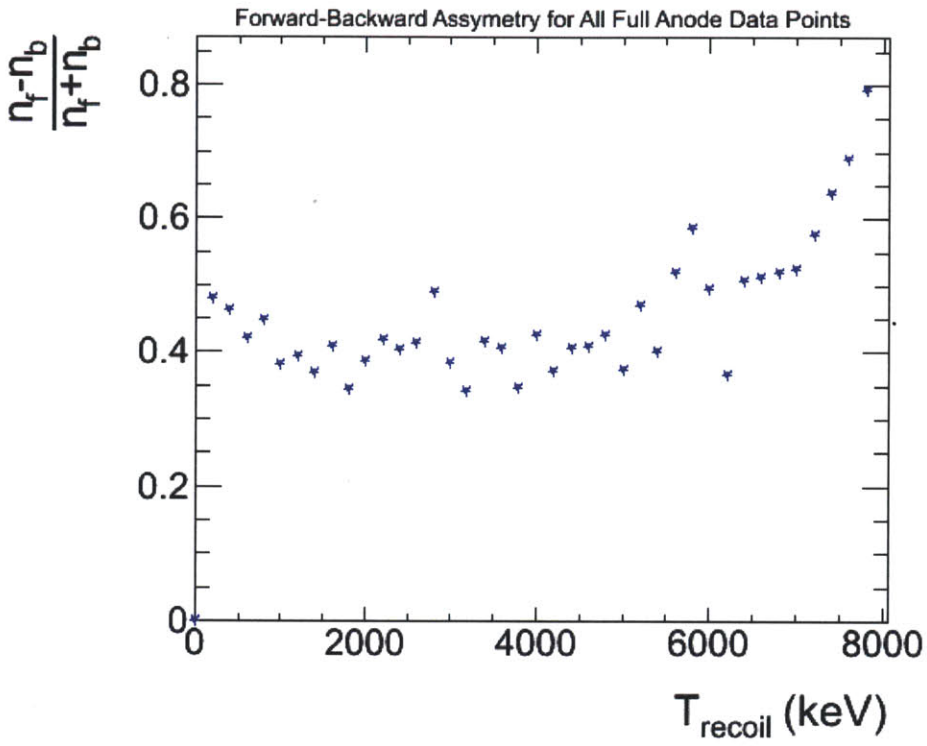

Figure 3-23: The head-tail assymetry for all data points of full anode imaging runs.

Chapter 4

Results

The process of scientific discovery is, in effect, a continual flight from wonder.

A. Einstein[24]

4.1 Results

The two greatest hurdles to overcome for this detector were imaging a full 30cm diameter anode at a distance which would allow a 50cm drift, and finding optimal amplification settings at pressurized helium. The Double Chooz collaboration had "difficulty finding suitable operating conditions for the 6.25% gas mixture," reporting large gain differences with small voltage variations[47]. The ability to operate at higher pressures is critical to increase the total cross section of this detector, and this paper presents successful tesing of the 6.25% gas mixture. The partial pressure of CF4 in a 6.25% gas mixture operated at 600 Torr, as in DCTPC, maintains the partial pressure of CF4 over the gap between the anode and ground mesh with one standard deviation of the most sensitive portion of the Paschen Curve [48]. Operating a 1120 Torr, the partial pressure of CF4 sits at 70 torr, maintaining well outside of the sensitive region of CF4 breakdown.

Probability Calculation s^{-1}	Geant4 Simulation s^{-1}	Actual Track Detection s^{-1}
2.2	2.1 ± 0.02	1.99 ± 0.01

Table 4.1: Total Track Detection Rate compared with Calculated and Simulated Rates between 0.1MeV and 4MeV

This detector returned results in very good agreement with the expected rates computed through probability-based rate calculations as well as a Geant4 simulation.

Assuming the simulation to have higher sensitivity to expected detection rate, the detector displayed a track detection efficiency of 95 %.

4.2 Future Work

Phase II of the development of this technology will incorporate a push for larger total cross section. Whether this is accomplished through the construction of a single cubic-meter detector or through multiple 250-L detectors, the end result will be a significant increase in track detection rate for similar sources at similar distances. Of note particular to the detector currently being discussed, with the construction of a triple-mesh setup (currently under development by the DMTPC collaboration), the exact same camera/lens setup could be used to image two drift regions as depicted in Fig. 4-1. The two mesh's are held at ground, while the central mesh is held at the same particular anode setting. Each drift region drifts inward to the central anode, with only one camera imaging both drift regions. This is a concept currently in development for the DMTPC collaboration. Further, as mentioned previously, the current setup wastes some of the EMCCD chip. The Phase II detector could maximize the size of the anode within the limitations of the current lens/camera setup, arriving at an anode that is 60% larger in area with no expected loss in signal or directional resolution. Further, if each drift region is extended to 55cm drift, the total volume

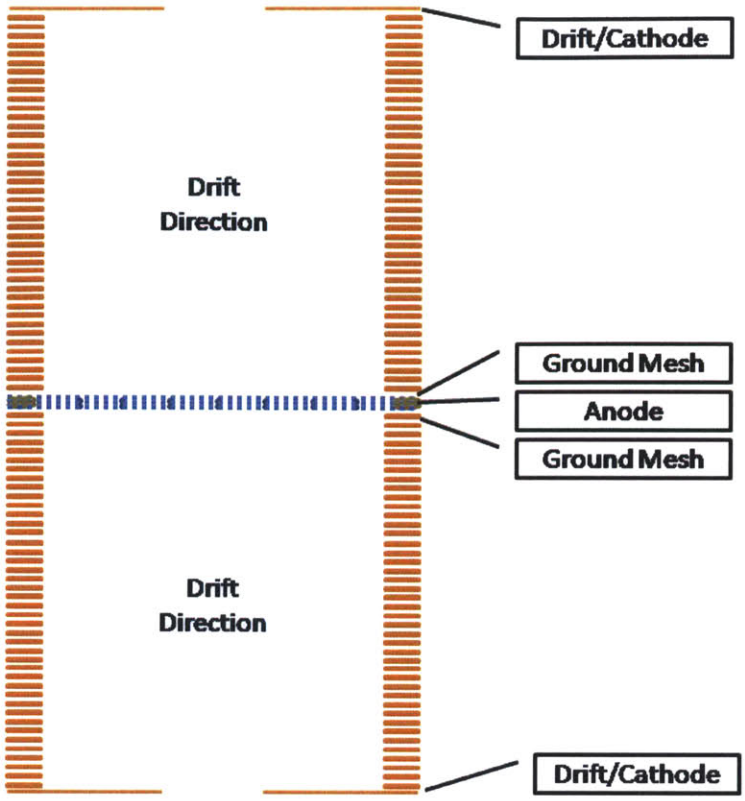

Figure 4-1: A cartoon diagram of a triple mesh design to image two drift regions, currently being developed by the DMPTC collaboration

for such a detector would be 130 liters. This would have the same performance of the current detector setup with alomst triple the target mass. Further, with such a chamber constructed to withstand pressures up to 5 bar, the target mass will be ten times the current target mass.

Additional studies should be conducted to test the difference between coincidence of two smaller detectors opposed to one large detector. Potentially, two smaller detectors placed in close proximity to a route of passage (in the form of a portal monitor) may detect a source passing in a slow moving vehicle through coincidence measurements in a shorter time than a single, large detector. If this is proven before the construction of a cubic meter detector, the detector setup mentioned earlier could serve as two portal monitor detectors with minimal additional research and develop-

ment, with a total height of 110 cm plus height of camera, and only 40 cm wide.

4.3 Conclusion

This detector presents a promising approach to detecting SNM or WGP with the appropriate considerations made to source distance, length of time to scan, and total detector size capability. With a track detection efficiency of 95% and minimal major improvements needed to scale to an immediate ten-fold in total target mass, the current technology ready to be further ruggedized and tested in the full spectrum of weather conditions and portal environments.

Bibliography

[1] A. Folsing. *Albert Einstein.* Penguin Books. New York, NY. 1997.

[2] *IAEA Publications: Factsheets and FAQs*, "Nuclear Non-Proliferation: Chronology of Key Events," [Online], Available: http://www.iaea.org/Publications/Factsheets/English/npt_chrono.html.

[3] K.T. Bainbridge. *Trinity.* U.S. Energy Research and Development Administration. May 1976.

[4] J. Bernstein, *Nuclear Physics.* Cambridge University Press: New York, NY. 2008.

[5] J. Marka, "Explosive Properties of Reactor-grade Plutonium," *Science and Global Security: The Technical Basis for Arms Control, Disarmament, and Non-proliferation Initiatives*, vol. 4, pp. 111-128, 1993.

[6] C. Sublette. "Section 2.0 Introduction to Nuclear Weapon Physics and Design." *Nuclear Weapons Frequently Asked Questions.* WWW Document. http://www.nuclearweaponarchive.org/Nwfaq/Nfaq2.html.

[7] B. C. Reed. *The Physics of the Manhattan Project.* Springer: Heidelberg, Germany, 2011.

[8] S. Fetter *et al.*, "Detecting Nuclear Warheads," *Science and Global Security: The Technical Basis for Arms Control, Disarmament, and NonProliferation Initiatives*, vol. 1, pp. 225-302, 1990.

[9] *Types of Nuclear Weapons.* [Online]. Available: (http://www.ctbto.org/nuclear-testing/types-of-nuclear-weapons/).

[10] S. Fetter, V. Frolov, O. Prilutsky, R. Sagdeev, "Fissile Materials and Weapon Design," *Science and Global Security: The Technical Basis for Arms Control, Disarmament, and NonProliferation Initiatives*, vol. 1, pp. 255-263, 1990.

[11] D. Hawkins, "The Los Alamos Project, Vol. 1: Inception until August 1945," *Manhattan District History Project Y*, Los Alamos Scientific Laboratory, Los Alamos, NM 1946.

[12] L. De Geer, "Nonintrusive Detection of Nuclear Weapons on Ships", *National Defence Research Establishment*, February 1990.

[13] L. Gerber. "The Baruch Plan and the Origins of the Cold War." *Diplomatic History.* vol. 6, pp. 69-96, 1982.

[14] H. L. Stimson. "The Decision to Use the Atomic Bomb." *Harper's Magazine.* vol. 194, pp. 97-107, 1947.

[15] "Emergency Committee of Atomic Scientists." *Nature.* vol. 159, no. 4051, pp. 837, 1947.

[16] D. Eisenhower, "Address Before the General Assembly of the United Nations on Peaceful Uses of Atomic Energy, New York City", *Public Papers of the President*, pp. 813-822.

[17] U.S. Congress, Office of Technology Assessment, *Technologies Underlying Weapons of Mass Destruction, OTA-BP-ISC-115* (Washington, DC: U.S. Government Printing Office, December 1993).

[18] T. Cochran, C. Paine, "The Amount of Plutonium and Highly-Enriched Uranium Needed for Pure Fission Nuclear Weapons," *Nuclear Weapons Databook*, Natural Resources Defense Council, Washington, D.C. 1995.

[19] R. Kouzes, "Detecting Illicit Nuclear Materials," *American Scientist*, vol. 93, no. 5, pp. 422-427, 2005.

[20] L. Wein, A. Wilkins, M. Baveja, S. Flynn, "Preventing the Importation of Illicit Nuclear Materials in Shipping Containers," *Risk Analysis*, vol. 26, no. 5, pp. 1377-1393, 2006.

[21] *Neutron Scattering Lengths and Cross Sections*, [Online], Available: http://www.ncnr.nist.gov/resources/n-lengths/.

[22] *Reference neutron radiations – Part 1: Characteristics and methods of production* "ISO 8529-1", 2001.

[23] S. Ahlen, *et al.*, "A Background-Free Direction-Sensitive Neutron Detector," *IEEE Transactions on Nuclear Science*, vol 57, issue 5, pp. 2740-2746.

[24] A. Calaprice, ed. *Teh Quotable Einstein*, Princeton University Press, Princeton, NJ 1996.

[25] S. Ahlen *et al.*, "First Dark Matter Search Results from a Surface Run of the 10-L DMTPC Directional Dark Matter Detector," *Physics Letters B*, vol. 695, pp. 124-129.

[26] D. Dujmic *et al.*, "Charge Amplification Concepts for Direction-Sensitive Dark Matter Detectors," *Astroparticle Physics*, vol. 30, issue 2, pp. 58-64, 2008.

[27] R. Madaras, P. Oddone, "Time-projection Chambers," *Physics Today*, vol. 37, issue 8, pp. 36-44.

[28] L. Christophrou, J. Olthoff, M. Rao, "Electron Interactions with CF4", *J. Phys. Chem. Ref. Data*, vol. 25, no. 5, pp. 1341-1388, 1996.

[29] I. C. Wolfe, "Measurement of Work Function in CF4 Gas", *Senior Thesis: Massachusetts Institute of Technology*, 2010.

[30] H. Burhop, "The De-Excitation of Helium Metastable Atoms in Helium", *Proc. Phys. Soc. A*, vol. 67, pp. 276-280, 1954.

[31] J. Pack, R. Voshall, A. Phelps, L. Kline, "Longitudinal Electron Diffusion Coefficients in Gases: Noble Gases," *Journal of Applied Physics*, vol. 71, issue 11, pp. 536-5371, 1992.

[32] A. Kaboth, *et al.*, "A Measurement of Photon Production in Electron Avalanches in CF4", *Nucl. Instr. and Meth. in Phys. Res. A*, vol. 592, pp. 63-72, 2008.

[33] J.Lopez *et al.*, "Background Rejection in the DMTPC Dark Matter Search Using Charge Signals," *Nuclear Instruments and Methods in Physics Research A*, vol. 696, pp. 121-128, 2012.

[34] Andor Technology, $iXon_3$ 888. [Online]. Connecticut. Available: http://www.andor.com/scientific-cameras/ixon-emccd-camera-series/ixon3-888.

[35] ProLine PL09000 Specification Sheet, Finger Lakes Instrumentation. [Online]. Lima, NY. Available: http://www.flicamera.com/proline/index.html.

[36] A. Barbieri, A. Chen, W. Koch, "A Novel Approach to the Observation of Cosmic Muons." In-class assignment. 8-811 Particle Physics II. Professor Markus Klute. December 2012.

[37] Synaccess: Remote Power and Console Management, [Online]. Available: http://www.synaccess-net.com/remote-power.php/1/3.

[38] Troxler: The Leader in Construction Testing Equipment, [Online]. Available: http://www.troxlerlabs.com/products/4301.php.

[39] G. Knoll, *Radiation Detection and Measurement: Fourth Edition*, Wiley, Ann Arbor, Michigan, 2010.

[40] *Evaluated Nuclear Data File(ENDF).* December 2011. [Online]. Available: http://www.nndc.bnl.gov/exfor/endf00.jsp.

[41] P. Rinard, *Neutron Interactions with Matter*, 1991.

[42] H. W. Taylor, *Cement Chemistry*, Thomas Telford Publishing, New York, NY. 1997.

[43] J. Beringer *et al.* (Particle Data Group), Phys. Rev. D86, 010001 (2012).

[44] J. Ziegler, "SRIM-2003", *Nuclear Instruments and Methods in Physics Research B*, vol. 219, pp. 1027-1036, 2004.

[45] S. Agostinelli, *et al.*, "Geant4: a Simulation Toolki", *Nuclear Instruments and Methods in Physics Research A,*, vol. 506, issue 3, pp. 250-303, 2003.

[46] J. Allison, *et al.*, "Geant4 Developments and Applications", *IEEE Transactions on Nuclear Science*, vol. 53, no. 1, pp. 270-278, 2006.

[47] J. Lopez, *et al.* "A Prototype Detector for Directional Measurement of the Cosmogenic Neutron Flux", *Nuclear Instruments and Methods in Physics Research A*, vol. 673, pp. 22-31, 2012.

[48] N. Skoro, G. Malovic, D. Maric, Z. Petrovie, "Low-pressure Breakdown and Voltage-Current Characteristics of DC Discharge in CF4", *28th ICPIG*, Prague, Czech Republic, 2007.

[49] T. Sato and K. Niita, "Analytical functions to predict cosmic-ray neutron spectra in the atmosphere" *Radiat. Res.* 166, 544-555 (2006).

[50] T. Sato, H. Yasuda, K. Niita, A. Endo and L. Sihver "Development of PARMA: PHITS-based Analytical Radiation Model in the Atmosphere" *Radiat. Res.* 170, 244-259 (2008).

[51] *EXPACS: Excel-based Program for calculating Atmospheric Cosmic-ray Spectrum.* April 2013. [Online]. Available: http://phits.jaea.go.jp/expacs/.

Appendix A

Probability Rate Calculation

The data for all neutron cross sections for each of the gas mixture nuclei was uploaded to a ROOT data analysis macro from the Evaluated Nuclear Data File at Brookhaven National Laboratory [40]. Each table was uploaded to a TGraph to be used in the calculations, with the data presented in Fig. A-1.

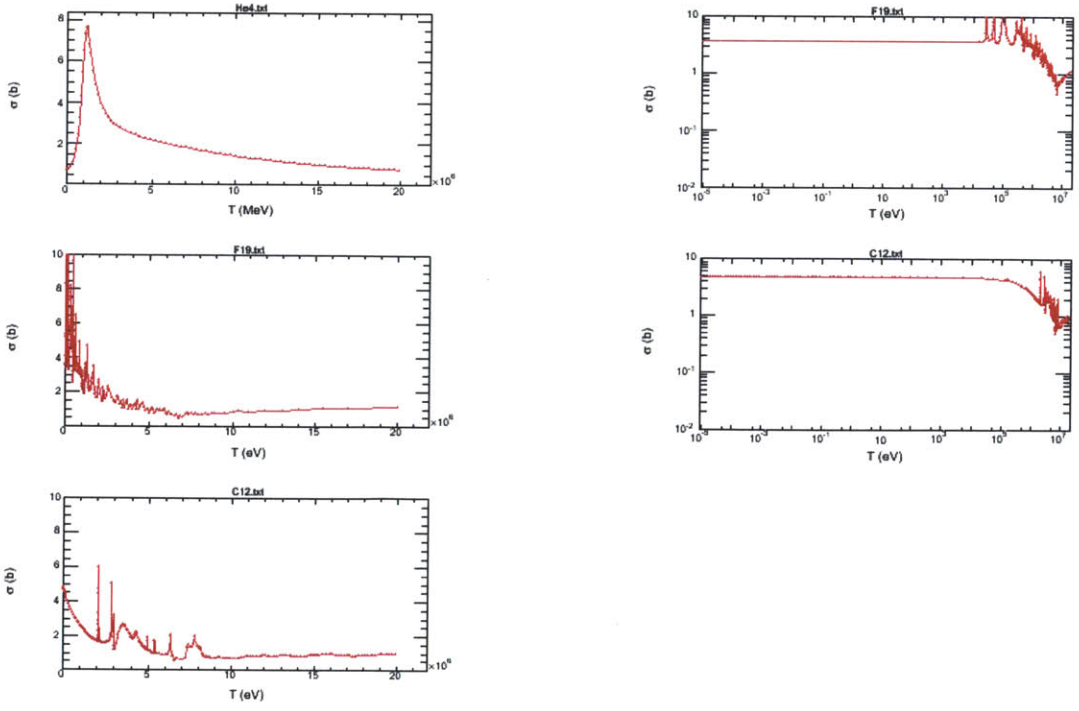

Figure A-1: Neutron Elastic Scatter Cross Section Data for Gas Mixture Nucleii

Additionally, the data describing the neutron energy spectrum for the Americium-Beryllium and Californium neutron sources were uploaded from an ISO technical report into the same ROOT data analysis macro and converted into TGraph's [22]. This data provided the flux as a function of energy, $\phi(E)$. These energy spectra are depicted in Figures A and A.

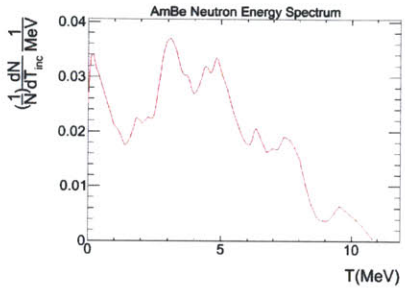

Figure A-2: The Experimental Neutron Energy Spectrum from an AmBe Neutron Source[22]

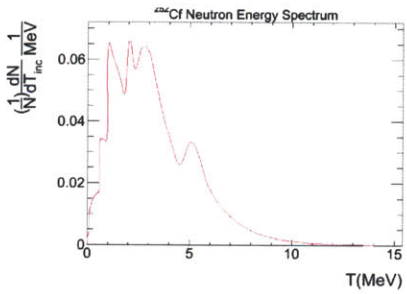

Figure A-3: The Experimental Neutron Energy Spectrum from an ^{252}Cf Neutron Source[22]

Using the energy spectrum and cross section plots as input, each possible incident energy bin is multiplied by the probability from the differential cross section and dispersed along the spectrum of recoil energies based on two-body kinematics. This three dimensional plot represents the differential probability as a function of incident energy and recoil energy, $\sigma(E', E)$. In a two-dimensional histogram, with recoil energy and incident energy as the X and Y axis, the Z-component becomes the probability. These plots are shown in Fig. A-4 for each recoil nucleii.

As can be seen in the differential cross section three-dimensional histograms, energies above $4 * \frac{T_{inc} * M_{target}}{(M_{target}+M_N)^2}$ are forbidden. Using these probabilities, the rate for each nucleii is computed as a function of energy by integrating over the incident energy at each recoil energy, as shown in Eqn. A.1.

$$\frac{d\sigma}{dT_{recoil}} = \int \sigma(E', E)\phi(E)\, \mathrm{d}E' \tag{A.1}$$

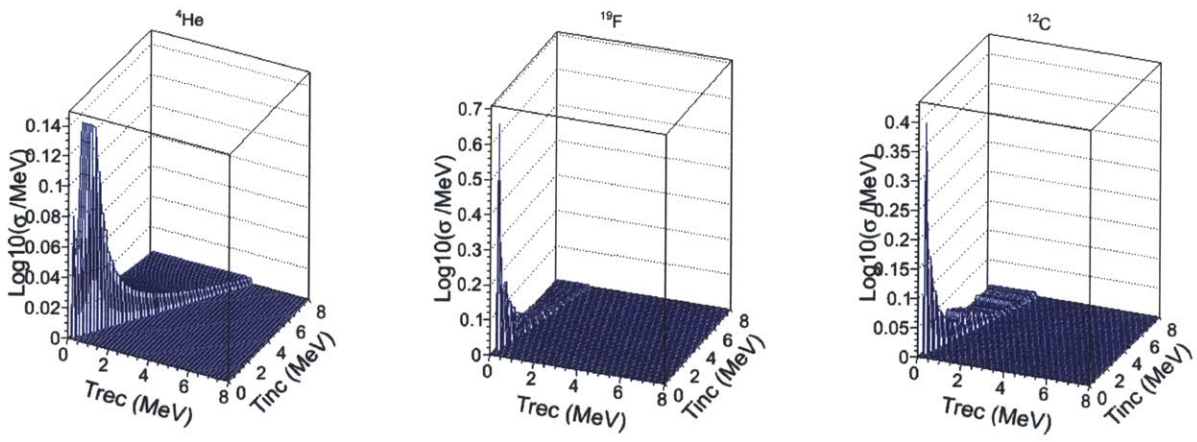

Figure A-4: The differential cross section for each possible incident neutron energy and recoil nucleii energy for each target nucleii (Left-^4He, Middle-^{19}F, Right-^{12}C)

Applying the ideal gas law, $PV = NRT$, to arrive at the density of target nucleii ρ in a given volume V, and the flux of neutrons given by the source activity A at a distance r returns an expected rate as a function of recoil energy from Eqn. A.2.

$$R(E) = \frac{1}{N}\frac{dN}{dT_{rec}} = \rho V \frac{A}{4\pi r^2}\frac{d\sigma}{dT_{recoil}} \tag{A.2}$$

The expected rate is re-produced for a AmBe source at 30cm from the sensitive volume of the detector in Fig A-5.

In order to compute an expected rate for the neutron background, the energy spectrum and rate were computed using the "Excel-based Program for Calculating Atmospheric Cosmic-ray Spectrum" (EXPACS) [49] [50] [51]. This provides a detailed interface to provide location, altitude, and surrounding environment in order to compute the cosmic-ray induced neutron background energy spectrum. The spectrum used for this calculation is reproduced below in Fig A-5.

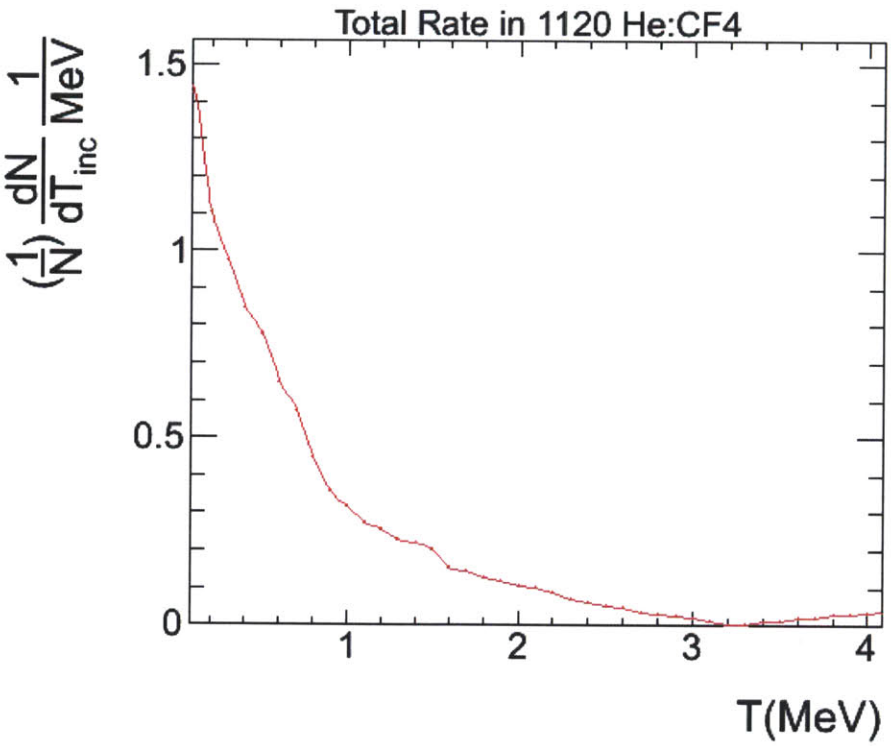

Figure A-5: The expected track detection rate for an AmBe source placed 30cm from a 1120 Torr 93.75% He / 6.25% CF4 gas mixture.